

# Spin-Flavor Precession Phase Effects in Supernova

T. Bulmus<sup>a</sup>, Y. Pehlivan<sup>a</sup>

<sup>a</sup>*Mimar Sinan Fine Arts University, Sisli, Istanbul, 34380, Türkiye*

---

## Abstract

We study the phase effects driven by neutrino magnetic moment for Majorana neutrinos in a core collapse supernova. A neutrino with a large magnetic moment is emitted in a superposition of energy eigenstates from the neutrinosphere. These energy eigenstates can interfere to create a phase effect at a partially adiabatic spin flavor precession (SFP) resonance. We examine the dependence of the SFP phase effect on the size of the neutrino magnetic moment as well as its variation with the post-bounce time. In particular, at late post-bounce times the SFP resonance becomes wider and eventually overlaps with the Mikheev-Smirnov-Wolfenstein (MSW) resonance. At this point Landau-Zener criteria for adiabaticity can no longer be applied to individual resonances, but we show that SFP phase effect is still present after the overlap. We also discuss the observability of the SFP phase effect at Deep Underground Neutrino Experiment (DUNE). Our analysis reveals that at low energies event rates do not fluctuate despite the presence of a sizable SFP phase effect. We find larger event rate fluctuations at high energies, but these fluctuations are also erased in the energy spectra of the observed charged leptons. A more refined treatment of electron fraction and the inclusion of neutrino-neutrino interactions may change our conclusions for observability in future studies.

*Keywords:* Neutrino magnetic moment, phase effects, supernova

---

## 1. Introduction

Neutrino's anomalous magnetic moment causes its spin to precess around a magnetic field [1–3]. This, coupled with the ordinary flavor evolution in vacuum, gives rise to the SFP phenomenon [4]. Ordinarily, the Standard Model predicts the neutrino magnetic moment to be of the order of  $10^{-20}\mu_B$  where  $\mu_B$  denotes the Bohr magneton [4, 5]. This value is too small to be consequential in most settings, but it is also possible that the neutrino magnetic moment is larger than the Standard Model prediction [6, 7]. Current experimental upper bound for neutrino magnetic moment is of the order of  $10^{-11}\mu_B$  [8]. However, somewhat stronger bounds can be provided with astrophysical arguments [9]. For a recent review of neutrino electromagnetic properties, see Ref. [10]. Here, we assume that the neutrino magnetic moment is of the order of  $10^{-16}\mu_B$  or larger.

If the magnetic field is perpendicular to the velocity of the neutrino, then spin precession causes neutrino's helicity to oscillate. As a result, SFP is modified in matter because positive and negative helicity neutrinos interact differently [11–14]. In particular, each interaction forces the neutrino back into a flavor state so that SFP is suppressed in high matter density. But, under the right conditions, the effects of the matter interactions and the vacuum oscillations can cancel each other. Around this cancellation region even a relatively weak magnetic field can cause significant helicity transformation, which is known as the SFP resonance [13, 14]. It is analogous to the MSW resonance which happens when neutrinos undergo ordinary flavor oscillations in a medium and a similar cancellation leads to significant

flavor transformation even for a very small mixing angle [15–17].

In this paper, we consider the phase effects driven by the neutrino magnetic moment and the associated SFP resonance in a core collapse supernova. We call this the *SFP phase effect* in order to distinguish it from the *ordinary phase effect* [18–20] associated with the standard flavor oscillations and the MSW resonances. The appearance of ordinary phase effect in a core collapse supernova is pointed out in many references [21–26] and examined in detail in Ref. [27]. Both the standard flavor oscillations and SFP can take place without the phase effects, whose development require two additional conditions to be satisfied in the given order: First, neutrinos should be evolving in superpositions of energy eigenstates, and second, they should pass through a partially adiabatic resonance. Partial adiabaticity is described by the Landau-Zener jumping probability [20, 28–31], and a Stoke's phase [32, 33]. It is the sum of the Stoke's phase and the relative phase acquired by the energy eigenstates during their evolution that creates the phase effects. Both the ordinary phase effect and the SFP phase effect emerge through the same underlying mechanism, but they differ in at least two important aspects to be discussed in what follows.

The ordinary phase effect appears when neutrinos go through two subsequent partially adiabatic MSW resonances in the same channel, which is often seen when the shock wave in a supernova creates a sharp local dip in matter density. In the usual scenario, the neutrino is produced nearly in an energy eigenstate at the center of the supernova. As it propagates, the first partially adiabatic MSW resonance transforms the neutrino into a superposition of two energy eigenstates and the second one creates the phase effect through an interference between them.

---

*Email address:* taygun.bulmus@msgsu.edu.tr (T. Bulmus)

In contrast, the SFP phase effect can appear even if there is only one partially adiabatic SFP resonance because, assuming it has a large magnetic moment, the neutrino is already produced in a superposition of energy eigenstates at the center. This is due to the fact that near the proto-neutron star, both the matter density and the magnetic field are expected to be high [34–36]. The strong magnetic field pulls the energy eigenstates close to the spin projection eigenstates along itself while the high matter density pulls them close to flavor eigenstates. As a result, a neutrino produced with a particular flavor and helicity is necessarily born into a superposition of energy eigenstates, which can subsequently interfere at the first partially adiabatic resonance.

Consequently, the first important difference between the ordinary phase effect and the SFP phase effect is in their ubiquity: The ordinary phase effect is limited to the part of the neutrino spectrum which experiences two partially adiabatic resonances in the same channel. The particulars of the shock wave propagation as well as the energy dependence of the adiabaticity parameter for the MSW resonances determine which part of the spectrum is effected. This can be seen, for example, in Fig. 2 of Ref. [21], Fig. 7 of Ref. [22], or Figs. 17-21 of Ref. [23]. In contrast, if it is present, the SFP phase effect affects the entire neutrino energy spectrum because a single SFP resonance is sufficient and its adiabaticity does not depend on the neutrino energy.

The second important difference between SFP phase effect and the ordinary phase effect involves the non-universal nature of the SFP resonance. MSW resonance is universal in the sense that its width in density scale is fixed by the vacuum mixing parameters. In contrast, the width of the SFP resonance depends on the way the magnetic field varies with respect to density. At late post-bounce times, it is possible that the SFP resonance becomes wide enough to overlap with the subsequent MSW resonance. Such an overlap breaks down the Landau-Zener formulation since it is only applicable to isolated resonances. We demonstrate that, after the overlap, the SFP phase effect continues to be present while both resonances appear to become adiabatic from a naive application of the Landau-Zener formulation.

Phase effects cause the neutrino survival and transition probabilities to oscillate with energy. These oscillations typically occur on very small scales so that the results may look randomized if the energy binning can not resolve them. In most cases, one eliminates the phase effects by averaging them out but there are also cases where it is important to understand them. For example, while discussing the impact of turbulence on neutrino oscillations, Ref. [25] points out to the interplay between turbulence and phase effects. In particular, it is shown that the impact of the turbulence can be numerically identified only when it starts to dominate over the phase effects, i.e., once it starts to create correlations in shorter energy scales than the phase effects.

The reason for the fast variation with energy is easy to understand in the case of non-overlapping resonances: According to the Landau-Zener approach, for each resonance channel the energy eigenstates can be considered pairwise and hence there is only one relevant phase difference in each case. Since this

phase difference is typically accumulated over a long distance (from production to the resonance or between two resonances) it is large and hence vary fast with energy. However, the picture is less clear when the SFP resonance wide enough to overlap with the MSW resonance. In this case, at least three energy eigenstates mix at the same time and hence there are two phase differences involved in the problem. Depending on the amount of overlap between the resonances, the accumulation distance can be shorter for at least one of these relative phases. Since an analytical treatment of the problem is challenging, it is difficult to make a purely theoretical deliberation at this point. For the model that we study, we find that the phase effects continue to be effective in small energy scales in the case of a partial overlap. However, we believe that this problem deserves to be investigated more systematically than we attempt in this paper.

From an observational point of view, capturing phase effects is challenging due to the finite detector energy resolutions. Ref. [27] concluded that the ordinary phase effect cannot be observed with the current detection capabilities. While we primarily focus on understanding the SFP phase effect, we also touch upon the possibility of observing it. We argue that when the oscillations of neutrino survival and transition probabilities occur on a small energy scale, it is more appropriate to think of them as random fluctuations within certain bounds because relative phases are also sensitive to small variations in external conditions. For this reason we treat the SFP phase effect as an *uncertainty* within which neutrino survival and transition probabilities can randomly fluctuate. Looking at the problem in this way leads to the conclusion that, irrespective of the detector energy resolution, phase effects cannot be observed if the neutrino flux is very high, e.g., at early post-bounce times. This is because if the detector captures many neutrinos in the same energy bin, then the random fluctuations would cancel each other in each one of them. On the other hand, if only a few neutrinos are captured in each energy bin as would be the case at late post-bounce times, then this cancellation may be partial and some residual randomization can remain. However, the latter can still be wiped out with imperfect detector energy resolution.

The technical details of our paper are as follows: We assume that neutrinos are Majorana particles and derive explicit analytical formulas to calculate the size of the uncertainties in survival and transition probabilities. This analytical treatment is valid for any density and magnetic field distribution as long as SFP and MSW resonances are decoupled in the sense that they do not overlap. In order to highlight a few basic features of the SFP phase effect, we first run illustrative simulations using an exponentially decreasing matter density and a magnetic field which decreases with the square of the distance from the center. In these illustrative simulations we mimic the effect of a shock wave by decreasing the central density with the post-bounce time. We show that the decoupling approximation (and our analytical treatment with it) fails at later post-bounce times due to the spreading of SFP resonance with dropping central density. This is especially true if the neutrino magnetic moment is large or if the magnetic field is strong. We also run simulations with a realistic density distribution based on a  $6M_{\odot}$  helium core presupernova model [37] and a parametric shock wave [21] to

demonstrate how the SFP phase effect may affect the survival and transition probabilities of neutrinos arriving Earth.

We start by reviewing the oscillations, precession and interactions of Majorana neutrinos inside the supernova in Section II. In Section III, we discuss SFP and MSW resonances, particularly focusing on the conditions under which they can be treated as two separate two-level problems. In Section IV, we discuss the adiabatic evolution of neutrinos inside the supernova, and their subsequent decoherence on their way to Earth. In Section V, we consider the hypothetical case of the zero vacuum mixing angle in order to remove the MSW resonance from the picture and focus on the phase effect between the production point and the SFP resonance. In Section VI, we consider the non-zero mixing angle case and thus include the MSW resonances. In Section VII, we discuss the observability of the SFP phase effect at late post-bounce times. In Section VIII, we present our discussion and conclusions.

## 2. Neutrinos inside the supernova

We work in the effective two flavor mixing scheme with 1-3 mixing parameters which is the relevant part of the full mixing parameter space for supernova. See, for example, Ref. [38] for three flavor effects. We denote the negative helicity flavor degrees of freedom by  $|\nu_e\rangle$  and  $|\nu_x\rangle$ . They respectively correspond to the electron flavor and an orthogonal flavor combination. Corresponding positive helicity states are respectively denoted by  $|\bar{\nu}_e\rangle$  and  $|\bar{\nu}_x\rangle$ . Majorana neutrinos are their own antiparticles but, as far as their production and detection are concerned, a positive helicity Majorana neutrino behaves very similar to a positive helicity Dirac antineutrino. For this reason, it is conventional to refer to Majorana neutrinos with positive helicities as antineutrinos. We also adopt this convention, but we refer to all degrees of freedom as neutrinos when no distinction is necessary.

A magnetic field turns a Majorana neutrino into a Majorana antineutrino by flipping its helicity. The resulting effect is described by the Hamiltonian<sup>1</sup>

$$H_\mu(r) = \mu B(r) (|\nu_e\rangle \langle \bar{\nu}_x| + |\bar{\nu}_x\rangle \langle \nu_e| - |\nu_x\rangle \langle \bar{\nu}_e| - |\bar{\nu}_e\rangle \langle \nu_x|). \quad (1)$$

This Hamiltonian only includes flavor off-diagonal terms because flavor-diagonal terms vanish identically due to the reality condition of the Majorana spinors [10, 39].  $B(r)$  in Eq. (1) denotes the component of the magnetic field perpendicular to the neutrino's direction of motion. For those neutrinos to be detected in experiments, it depends on the orientation of the supernova with respect to Earth in addition to the particulars of the supernova dynamics. For this reason, it is difficult to be specific about  $B(r)$ . Moreover, it is always the  $\mu B(r)$  combination which appears in equations. We find that, for the purposes of this paper the important parameters are the values of  $\mu B$  on the surface of the neutrinosphere and around the SFP resonance

<sup>1</sup>We use outer products rather than matrices because writing down  $4 \times 4$  matrices is impractical in the two-column format.

region. In particular, how the magnetic field changes in between these two points is less important. For definiteness, we use a magnetic field which decreases with the distance  $r$  from the center of the supernova as [40–43]

$$B(r) = B_0 \left( \frac{r_{\text{mag}}}{r} \right)^2 \quad (2)$$

where  $r_{\text{mag}} = 50$  km. Neutrino flavor evolution starts from the surface of the proto-neutron star which we also take to be at  $R = 50$  km. Therefore,  $B_0$  is effectively the magnetic field on the surface of the neutrinosphere. Its value can range from a conservative  $10^{12}$ G to extreme values such as  $10^{16}$ G [35, 44]. For example, taking  $B_0 = 10^{15}$ G and  $\mu = 3 \times 10^{-16} \mu_B$  leads to an energy separation of

$$\mu B_0 = 1.7 \times 10^{-9} \text{ eV} \quad (3)$$

between the helicity eigenstates on the surface of the neutrinosphere. This is larger than the typical separation of  $10^{-11}$  eV between neutrino mass eigenstates in vacuum but smaller than the typical separation of  $10^{-8}$  eV between the flavor eigenstates in matter. We discuss these figures below.

Neutrinos interact with other particles and with each other in the supernova [45, 46]. Here, we ignore the neutrino-neutrino interactions<sup>2</sup>. The interactions with the other particles can be further limited to the forward scattering alone because these are the only terms which add up coherently [15]. At the MeV energy scale relevant for the supernova, all weak interactions can be treated within the Fermi four point model in terms of the Fermi coupling constant  $G_F$ . With these considerations, the Hamiltonian describing the vacuum oscillations and interactions in an unpolarized neutral medium can be written as

$$\begin{aligned} H_{\nu \leftrightarrow \nu}(r) = & \left( -\frac{\delta m^2}{2E} \cos 2\theta + \frac{\sqrt{2}G_F n(r)}{m_n} \frac{3Y_e - 1}{2} \right) |\nu_e\rangle \langle \nu_e| \\ & + \left( \frac{\delta m^2}{2E_\nu} \cos 2\theta - \frac{\sqrt{2}G_F n(r)}{m_n} \frac{1 - Y_e}{2} \right) |\nu_x\rangle \langle \nu_x| \\ & + \frac{\delta m^2}{2E_\nu} \sin 2\theta (|\nu_e\rangle \langle \nu_x| + |\nu_x\rangle \langle \nu_e|) \end{aligned} \quad (4)$$

for neutrinos and

$$\begin{aligned} H_{\bar{\nu} \leftrightarrow \bar{\nu}}(r) = & \left( \frac{\delta m^2}{2E_\nu} \cos 2\theta + \frac{\sqrt{2}G_F n(r)}{m_n} \frac{1 - Y_e}{2} \right) |\bar{\nu}_x\rangle \langle \bar{\nu}_x| \\ & + \left( -\frac{\delta m^2}{2E_\nu} \cos 2\theta - \frac{\sqrt{2}G_F n(r)}{m_n} \frac{3Y_e - 1}{2} \right) |\bar{\nu}_e\rangle \langle \bar{\nu}_e| \\ & + \frac{\delta m^2}{2E_\nu} \sin 2\theta (|\bar{\nu}_e\rangle \langle \bar{\nu}_x| + |\bar{\nu}_x\rangle \langle \bar{\nu}_e|) \end{aligned} \quad (5)$$

for antineutrinos. Here, the terms involving the angle  $\theta$  represent the vacuum mixing of flavor eigenstates.  $E_\nu$  denotes the

<sup>2</sup>Neutrino-neutrino interactions turn the neutrinos streaming out of a supernova into a self interacting many-body system [47, 48] with non-linear behavior. See Ref. [49–51] for review. Without a large neutrino magnetic moment, the effects of the neutrino-neutrino interactions on neutrino flavor evolution is extensively studied. For normal mass hierarchy (NH) these interactions generally have minimal effect on the flavor evolution. For inverted mass hierarchy (IH) they cause different flavors to swap parts of their energy spectra with each other in the first few hundred km. With a large neutrino magnetic moment, the possible effects are more complicated. See, for example, Refs. [39–43]. We comment on how they can affect our results in the Conclusions.

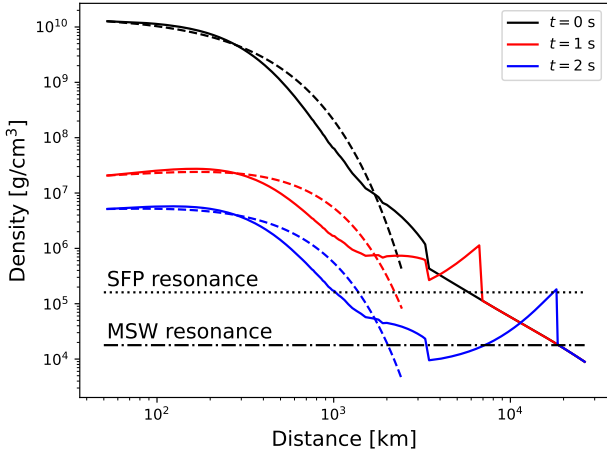


**Figure 1:** The density versus distance inside the supernova. The solid black line shows the density of the  $6M_{\odot}$  helium core presupernova model taken from Ref. [37]. The solid red and blue lines show the parametric shock wave superimposed on the presupernova distribution as described in Ref. [21] at  $t = 1$  s and  $t = 2$  s, respectively. The dashed lines in corresponding colors show the fitted density distributions described by Eqs. (7) and (8). For later post-bounce times, the results are close to the blue lines and not shown here. The horizontal lines show the SFP and MSW resonance densities for a 1 MeV neutrino.

neutrino energy, and  $\delta m^2$  denotes the squared difference of the two neutrino masses. In NH we have  $\delta m^2 > 0$  whereas in IH we have  $\delta m^2 < 0$ . For the 13 mixing parameters adopted here, we have  $\sin 2\theta = 0.29$  and

$$\frac{|\delta m^2|}{2E_{\nu}} = \frac{6.4 \times 10^{-11} \text{ eV}}{E_{\nu}/10 \text{ MeV}}, \quad (6)$$

which is the energy separation between mass eigenstates in vacuum.

In Eqs. (4) and (5), the environment is characterized by its mass density  $n(r)$  and its electron fraction  $Y_e$ . The electron fraction is defined as the ratio of electron and baryon number densities.  $m_n$  denotes the average baryon mass. In our calculations we assume slightly neutron rich conditions by taking  $Y_e = 0.45$ . The density profile that we use is based on the  $6M_{\odot}$  helium core presupernova model of Ref. [37]. We adopt this as the density distribution at the shock bounce at  $t = 0$ . At later times, the shock wave modifies the density profile. We mimic this by parametrically changing the  $t = 0$  matter density as described in Ref. [21] for up to post-bounce time  $t = 5$  s. We do this by using same shock wave speed and contact discontinuity parameters as in Ref. [21]. The resulting density distributions are shown in Fig. 1 with solid lines. These are the density distributions that we later use for our realistic calculations in Section VII. But, before that we run some illustrative simulations by fitting these density distributions to the functional form

$$n(r) = n_0 e^{-r/r_{\text{mat}}}. \quad (7)$$

We find that, at all post-bounce times and for the first few thousand kilometers, Eq. (7) fits the density distributions reasonably

well with  $r_{\text{mat}} = 200$  km and with different central densities at different post-bounce times. At  $t = 0$ , the central density is  $n_0 = 1.0 \times 10^{10}$  g/cm<sup>3</sup>. At later times we have

$$n_0 = \begin{cases} 1.8 \times 10^7 \text{ g/cm}^3 & t = 1 \text{ s}, \\ 4.4 \times 10^6 \text{ g/cm}^3 & t = 2 \text{ s}, \\ 2.3 \times 10^6 \text{ g/cm}^3 & t = 3 \text{ s}, \\ 1.5 \times 10^6 \text{ g/cm}^3 & t = 4 \text{ s}, \\ 1.0 \times 10^6 \text{ g/cm}^3 & t = 5 \text{ s}. \end{cases} \quad (8)$$

The fitted densities are also shown in Fig. 1 with dashed lines. The practical reason for using the fitted distributions in illustrative simulations is the necessity of running a large number of simulations in order to discuss various features of the phase effect. But another rationale is the fact that the SFP phase effect actually takes place in the density scale: the results mostly depend on the value of the magnetic field at a particular density rather than how the density and magnetic field are spread over the physical space. In other words, it is the interplay between the matter profile and the magnetic field profile that matters. It is in that sense that Eqs. (2) and (7) serve as a basis for illustration. For example, Fig. 1 clearly shows that, in the realistic case, the density decreases more slowly and the resonances take place in outer regions where the magnetic field is weaker. For this reason, a sizable SFP phase effect requires either a larger magnetic field or a larger neutrino magnetic moment in the realistic case than it is in the illustrative case. A shortcoming associated with using the exponential fits is that this approach reduces the post-bounce supernova dynamics to one variable, which is the central density given in Eq. (8). In particular, with the fitted densities neutrinos pass through MSW resonance only once whereas with actual densities some neutrinos pass it three times. However, as we discuss further in the Conclusions, additional resonances can only serve to increase the uncertainties associated with SFP phase effect.

On the surface of the proto-neutron star, the energy separation between flavor eigenstates created by the interactions is of the order of

$$7.8 \times 10^{-9} \text{ eV} \leq \frac{\sqrt{2}G_F n_0}{m_n} (1 - 2Y_e) \leq 1.4 \times 10^{-7} \text{ eV}, \quad (9)$$

where the minimum value corresponds to  $t = 1$  s and the maximum value corresponds to  $t = 5$  s. Comparing Eq. (9) with Eq. (3) one might think that the importance of the SFP phase effects increases at later post-bounce times. However, as we discuss below, the situation is less straightforward.

### 3. The Resonances

Since neutrinos of all flavors are emitted from the neutrinosphere, it is better to work with a density operator rather than individual initial states. We denote by  $\hat{\rho}(E_{\nu}, r)$  the normalized density operator which describes all neutrinos and antineutrinos with energy  $E_{\nu}$  which are at a distance  $r$  from the center of the supernova. The energy dependence of  $\hat{\rho}(E_{\nu}, r)$  comes in part from vacuum oscillations as shown in Eq. (6), and in

part from the energy dependence of emission from the neutrinosphere. For brevity, we suppress the energy dependence of the density operator unless it is necessary for discussion. But whenever we write  $\hat{\rho}(r)$ , a specific neutrino energy is always implied.

We assume that all neutrinos represented by the density operator  $\hat{\rho}(r)$  are emitted from the surface of the neutrinosphere at the same time and traveled outward with the speed of light to reach  $r$ . This is a simplification because in reality every point on the surface of the neutrinosphere emits neutrinos uniformly in every direction pointing outward. Even in a spherically symmetric supernova, which we assume to be the case, neutrinos would travel by slightly different distances and experience slightly different conditions depending on their direction of emission. Ignoring this dependence is called the single angle approximation<sup>3</sup> and it effectively reduces the problem to the one dimensional evolution equation

$$i \frac{d}{dr} \hat{\rho}(r) = [H(r), \hat{\rho}(r)]. \quad (10)$$

Here the flavor evolution is described in terms of the distance  $r$  because neutrinos essentially travel with the speed of light. Most of the non-trivial flavor evolution takes place by the time neutrinos reach the low density outer layers of the supernova, which takes only a fraction of a second. This is much shorter than the time scale with which the supernova background changes. For this reason, one can take a snapshot of the supernova at the post-bounce time  $t$ , put this information into the Hamiltonian  $H(r)$  in Eq. (10) and solve it to find the flavor evolution of the neutrinos that are emitted at time  $t$ . In this sense, Eq. (10) depends on the post-bounce time  $t$ . This dependence is not explicitly shown in our equations, but we solve Eq. (10) for the post-bounce times from  $t = 1$  s to  $t = 5$  s and clearly label the corresponding results.

The total Hamiltonian  $H(r)$  includes the vacuum oscillations of neutrinos, their interactions with the matter background, and the effect of the magnetic field. It can be written as

$$H(r) = H_{\nu\leftrightarrow\nu}(r) + H_{\bar{\nu}\leftrightarrow\bar{\nu}}(r) + H_{\mu}(r) \quad (11)$$

with the individual terms given by Eqs. (1), (4) and (5). The evolution described by Eqs. (10) and (11) is not difficult to solve numerically. However, much insight can be gained by analytically examining its evolution under adiabatic conditions. In general, adiabaticity refers to a situation where the external conditions affecting a system change slowly in comparison to the system itself. For the problem at hand, this means that the distance scales over which the matter density and the magnetic field change should be much longer than the distance scale over which the neutrino oscillates. Adiabatic evolution can be described in a simple way in terms of the energy eigenstates of the Hamiltonian: An initial state which is nearly an energy

<sup>3</sup>The geometry of this approximation is studied in detail in Ref. [52]. The focus of this reference is the neutrino-neutrino interactions, but its geometrical treatment of neutrinos emitted in all directions from a spherical source can be generally applied.

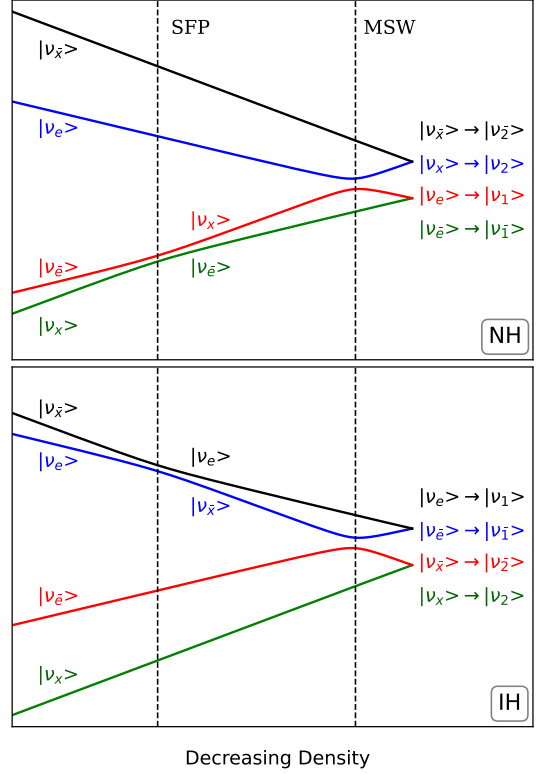


**Figure 2:** The energy eigenvalues of the total Hamiltonian as functions of the logarithm of the density, which decreases from left to right. The figure is independent of the density distribution model. Dominant flavor contents of the corresponding eigenstates are indicated next to the lines. On the right, we show the flavor contents of the eigenstates right after the MSW resonance and to which mass eigenstates they adiabatically evolve in vacuum.

eigenstate evolves approximately into the same eigenstate at later times. We can quantify this by denoting the local energy eigenvalues of the total Hamiltonian in Eq. (11) by  $E_i(r)$  and the corresponding energy eigenstates by  $|r_i\rangle$ . In other words, at every point  $r$ , we have

$$\hat{H}(r) = \sum_{i=1}^4 E_i(r) |r_i\rangle \langle r_i|. \quad (12)$$

We order the eigenvalues such that  $E_1$  is the largest and  $E_4$  is the smallest. The adiabaticity condition can be expressed as

$$\left| \langle r_i | \frac{dH(r)}{dr} | r_j \rangle \right| \ll |E_i(r) - E_j(r)|. \quad (13)$$

As long as the adiabaticity requirement is met, the evolution is determined solely by the energy spectrum of the Hamiltonian. The adiabatic approximation tells us that if the initial state of a neutrino on the neutrinosphere ( $r = R$ ) is an energy eigenstate  $|R_i\rangle$ , then it evolves into

$$|R_i\rangle \rightarrow e^{-i \int_R^r E_i(r) dr} |r_i\rangle \quad (14)$$

at a later time.

Fig. 2 shows the eigenvalues of the Hamiltonian as functions of the logarithm of the density. Since the eigenvalues are plotted against density, the actual density distribution is irrelevant. The two points where the eigenvalues approach to each other pairwise are SFP and MSW resonance points. These are the points at which the adiabaticity condition comes closest to being violated. If an adiabaticity violation occurs, one speaks of a partially adiabatic resonance. In partially adiabatic case, even if the initial state is approximately an energy eigenstate, it evolves into a superposition of the two approaching energy eigenstates as described by the Landau-Zener jumping probability [28–30] to be discussed below. As the density decreases from the center, the first resonance occurs between  $E_4$  and  $E_3$  for NH, and between  $E_1$  and  $E_2$  for IH. On the other hand, near the central regions the density is large enough to force each energy eigenstate to significantly project on a particular flavor eigenstate. The dominant flavor content of each energy eigenstate is indicated in Fig. 2. In particular, noting that  $3Y_e - 1 < 1 - Y_e$  for the neutron rich conditions ( $Y_e < 1/2$ ), and substituting the numerical values given in Eqs. (3), (6), and (9), into the Hamiltonians (4) and (5), we find

$$(|R_1\rangle, |R_2\rangle, |R_3\rangle, |R_4\rangle) \approx (|\bar{\nu}_x\rangle, |\nu_e\rangle, |\bar{\nu}_e\rangle, |\nu_x\rangle) \quad (15)$$

in both hierarchies on the neutrinosphere. In that sense, one can loosely say that the SFP resonance occurs between  $\bar{\nu}_e - \nu_x$  in NH, and between  $\nu_e - \bar{\nu}_x$  in IH. Indeed, one can re-write the Hamiltonian in Eq. (11) in the following decomposition:

$$H(r) = H_{e\leftrightarrow\bar{x}}(r) + H_{x\leftrightarrow\bar{e}}(r) + H_\theta. \quad (16)$$

Here,  $H_{e\leftrightarrow\bar{x}}(r)$  and  $H_{x\leftrightarrow\bar{e}}(r)$  are the parts of the Hamiltonian in Eq. (11) which live in the orthogonal  $\nu_e - \bar{\nu}_x$  and  $\bar{\nu}_e - \nu_x$  subspaces, respectively. They are given by

$$\begin{aligned} H_{e\leftrightarrow\bar{x}}(r) = & -\left(\frac{\delta m^2}{4E} \cos 2\theta - \frac{\sqrt{2}G_F n(r)}{m_n} \frac{3Y_e - 1}{2}\right) |\nu_e\rangle \langle \nu_e| \\ & + \left(\frac{\delta m^2}{4E} \cos 2\theta + \frac{\sqrt{2}G_F n(r)}{m_n} \frac{1 - Y_e}{2}\right) |\bar{\nu}_x\rangle \langle \bar{\nu}_x| \\ & + \mu B (|\nu_e\rangle \langle \bar{\nu}_x| + |\bar{\nu}_x\rangle \langle \nu_e|) \end{aligned} \quad (17)$$

and

$$\begin{aligned} H_{\bar{e}\leftrightarrow x}(r) = & -\left(\frac{\delta m^2}{4E} \cos 2\theta + \frac{\sqrt{2}G_F n(r)}{m_n} \frac{3Y_e - 1}{2}\right) |\bar{\nu}_e\rangle \langle \bar{\nu}_e| \\ & + \left(\frac{\delta m^2}{4E} \cos 2\theta - \frac{\sqrt{2}G_F n(r)}{m_n} \frac{1 - Y_e}{2}\right) |\nu_x\rangle \langle \nu_x| \\ & - \mu B (|\nu_x\rangle \langle \bar{\nu}_e| + |\bar{\nu}_e\rangle \langle \nu_x|). \end{aligned} \quad (18)$$

These two Hamiltonians describe flavor transition in two orthogonal channels. The term  $H_\theta$  in Eq. (16) is given by

$$H_\theta = \frac{\delta m^2}{2E_\nu} \sin 2\theta (|\nu_e\rangle \langle \nu_x| + |\nu_x\rangle \langle \nu_e| + |\bar{\nu}_e\rangle \langle \bar{\nu}_x| + |\bar{\nu}_x\rangle \langle \bar{\nu}_e|)$$

and it couples these two orthogonal channels. Since  $H_\theta$  is proportional to the small term  $\frac{\delta m^2}{2E_\nu} \sin \theta$ , its effect can be ignored near the neutrinosphere. In this case, the spin-flavor evolution proceeds through the decoupled  $\nu_e - \bar{\nu}_x$  and  $\bar{\nu}_e - \nu_x$  channels. This is what we see on the high density part of Fig. 2 where

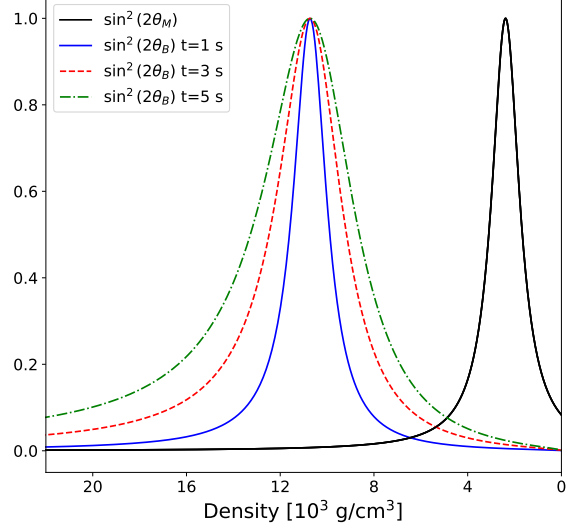


**Figure 3:** Resonance widths as represented by effective mixing angles at different post-bounce times. The density decreases from left to right. The solid black line shows  $\sin^2 2\theta_M(r)$  corresponding to the MSW resonance, whose universality means that its position and width is the same in density scale at all post-bounce times. The solid blue, dashed red, and dash-dotted green lines show  $\sin^2 2\theta_B(r)$  for SFP resonance at post-bounce times  $t = 1, 3, 5$  s, respectively. While SFP resonance occurs at a fixed density, its physical location moves to inner regions at later post-bounce times where the magnetic field is stronger. For this reason it becomes wider with time. The figure is for a 15 MeV neutrino with exponentially fitted density distributions. The value of  $\mu B_0$  given by Eq. (3) is used. For smaller  $\mu B_0$ , the SFP resonance is narrower.

the large energy separation between the upper and lower pairs of eigenvalues forbids the transition between them. In this decoupling approximation, SFP resonance occurs when the diagonal elements of the Hamiltonians in Eqs. (17) or (18) become equal. This happens when [13, 14]

$$\frac{\delta m^2}{2E_\nu} \cos 2\theta = \pm \frac{\sqrt{2}G_F n(r)}{m_n} (1 - 2Y_e), \quad (19)$$

where  $-$  sign is for  $H_{e\leftrightarrow\bar{x}}(r)$  and  $+$  sign is for  $H_{\bar{e}\leftrightarrow x}(r)$ . Clearly, for  $Y_e < 0.5$  adopted in this paper, the condition in Eq. (19) can hold only for the former in NH, and only for the latter in IH. In the rest of this paper, we focus on NH. When the effect of the  $H_\theta$  is included the location of the SFP resonance shifts as discussed in Ref. [53]. But for the small mixing angle that we use, this is inconsequential.

In the decoupling limit, Eq. (18) tells us that the lower two eigenstates which undergo SFP resonance are combinations of  $|\nu_x\rangle$  and  $|\bar{\nu}_e\rangle$ . This can be expressed in terms of an effective mixing angle:

$$\begin{aligned} |r_3\rangle &= \cos \theta_B(r) |\nu_x\rangle + \sin \theta_B(r) |\bar{\nu}_e\rangle, \\ |r_4\rangle &= -\sin \theta_B(r) |\nu_x\rangle + \cos \theta_B(r) |\bar{\nu}_e\rangle. \end{aligned} \quad (20)$$

Here the effective mixing angle  $\theta_B(r)$  is defined in the range  $0 \leq \theta_B(r) \leq \pi/2$  with

$$\tan 2\theta_B(r) = \frac{2\mu B(r)}{\frac{\delta m^2}{2E} \cos \theta - \frac{\sqrt{2}G_F n(r)}{m_n} (1 - 2Y_e)}. \quad (21)$$



Well above the resonance density,  $\theta_B(r) \simeq \pi/2$  so that the eigenstates are  $|r_3\rangle \simeq |\bar{\nu}_e\rangle$  and  $|r_4\rangle \simeq -|\nu_x\rangle$  as expected from Fig. 2. Well below the resonance density  $\theta_B(r) \simeq 0$  in which case the flavor contents of eigenstates are switched as is also shown in Fig. 2. At the resonance density where  $\theta_B = \pi/4$ , the energy eigenstates are maximal mixtures of flavor eigenstates. In that sense

$$\sin^2 2\theta_B(r) = 4 \sin^2 \theta_B(r) \cos^2 \theta_B(r) \quad (22)$$

can be used a measure of the width of the resonance because it will be different from zero as long as energy eigenstates are mixtures of flavor eigenstates. This quantity is plotted in Fig. 3 against density at different post-bounce times. The solid blue line is for  $t = 1$  s, the red dashed line is for  $t = 3$  s, and green dashed-dotted line for  $t = 5$  s. The points at which  $\sin^2 2\theta_B = 1$  (i.e., the resonance points) coincide because the plot is in density scale and SFP resonance occurs at a specific density. But the physical location of the SFP resonance moves closer to the center of the supernova at later post-bounce times as the overall density drops. This can also be seen in Fig. 1 where the horizontal line representing the SFP resonance crosses the density distributions at increasingly smaller radii. While this is true for both the realistic and the fitted density distributions, the latter is used in Fig. 3. An important observation is that the SFP resonance region, i.e. the region for which  $\sin^2 2\theta_B(r)$  is significantly different from zero, becomes increasingly wider in density scale at later post-bounce times. It happens because as the resonance moves inward it occurs in a region where the magnetic field is stronger. According to Eq. (21) a stronger magnetic field at a given density means a larger  $\theta_B(r)$ . The widening of SFP resonance with post-bounce time will be important in what follows. However, there is no similar widening effect for the MSW resonance.

MSW resonance occurs in the outer regions where the magnetic field is weaker. For this reason,  $H_\mu(r)$  can be ignored in the decomposition given by Eq. (11) so that the neutrino and antineutrino oscillations decouple. In this case, Fig. 2 tells us that the dynamics of  $|r_1\rangle - |r_4\rangle$  decouple from the dynamics of  $|r_2\rangle - |r_3\rangle$  in both hierarchies. With this approximation, MSW resonance occurs when the diagonal elements of  $H_{\nu\leftrightarrow\nu}(r)$  or  $H_{\bar{\nu}\leftrightarrow\bar{\nu}}(r)$  become equal, i.e. when

$$\frac{\delta m^2}{2E_\nu} \cos 2\theta = \pm \frac{\sqrt{2}G_F n(r)}{m_n} Y_e. \quad (23)$$

Here the + sign is for neutrinos and – signs is for antineutrinos. Resonance condition in Eq. (23) holds only for neutrinos in NH, and only for antineutrinos in IH. Since we focus on NH, the resonating eigenstates can be written as

$$\begin{aligned} |r_2\rangle &= \cos \theta_M(r) |\nu_e\rangle + \sin \theta_M(r) |\nu_x\rangle, \\ |r_3\rangle &= -\sin \theta_M(r) |\nu_e\rangle + \cos \theta_M(r) |\nu_x\rangle \end{aligned} \quad (24)$$

in terms of an effective matter mixing angle  $\theta_M(r)$  defined in the range  $0 \leq \theta_M(r) \leq \pi/2$  and given by

$$\tan 2\theta_M(r) = \frac{\frac{\delta m^2}{2E_\nu} \sin 2\theta}{\frac{\delta m^2}{2E_\nu} \cos 2\theta - \frac{\sqrt{2}G_F n(r)}{m_n} Y_e}. \quad (25)$$

The quantity  $\sin^2 2\theta_M(r)$  is similarly a measure of the resonance width and is plotted in Fig. 3. Like the SFP resonance, the MSW resonance occurs at the same position in density scale but physically moves inward with time. However, unlike the SFP resonance its width is fixed in density scale. This is because at a given density the value of  $\theta_M(r)$  depends only on the vacuum mixing parameters. This is referred to as the universality. For a detailed discussion, see, for example, Ref. [54]. The MSW resonance is universal in the sense that its width depends only on the vacuum mixing parameters at the density scale, not on how this density is spread in physical space. In that sense SFP resonance is not universal because its width depends on how the magnetic field changes with respect to the density.

The above description relies on the decoupling of the  $|r_1\rangle - |r_2\rangle$  and  $|r_3\rangle - |r_4\rangle$  dynamics in the SFP resonance region, and the decoupling of  $|r_1\rangle - |r_4\rangle$  and  $|r_2\rangle - |r_3\rangle$  dynamics in the MSW resonance region. These two approximations are not independent. They are both true when SFP and MSW resonances are well separated, and they both fail when these resonances are not well separated. The eigenstate  $|r_3\rangle$  which enters both resonances is the culprit here. We write  $|r_3\rangle$  as a combination of  $|\nu_x\rangle$  and  $|\bar{\nu}_e\rangle$  around the SFP resonance in Eq. (20), and as a combination of  $|\nu_x\rangle$  and  $|\nu_e\rangle$  around the MSW resonance in Eq. (24). Obviously both equations can be true only if  $\sin^2 2\theta_B(r)$  drops nearly to zero by the time  $\sin^2 2\theta_M(r)$  starts to become different from zero. Otherwise  $|r_3\rangle$  has to be combination of  $|\nu_x\rangle$ ,  $|\bar{\nu}_e\rangle$ , and  $|\nu_e\rangle$ . Therefore there is only one decoupling approximation, and it is the decoupling of the SFP and MSW resonances as quantified by their widths. Fig. 3 tells us that in general the decoupling approximation can be valid at early post-bounce times, but likely to fail at late post-bounce times. The degree to which it fails depends on how the magnetic field changes with respect to matter density, and how large the neutrino magnetic moment is because SFP resonance width is directly controlled by the value of  $\mu B(r)$  around the resonance region.

#### 4. Evolution and Decoherence

In what follows, we first consider electron antineutrino survival probabilities. This serves to illustrate the appearance of SFP phase effect and discuss its relative importance under different settings. We work with electron antineutrinos because they undergo SFP resonance in NH. To do this, we start with a pure ensemble of electron antineutrinos represented by the initial density operator

$$\hat{\rho}(E_\nu, R) = |\bar{\nu}_e\rangle \langle \bar{\nu}_e| \quad (26)$$

and then calculate its evolution. If the density operator evolves into  $\hat{\rho}(E_\nu, r)$  at  $r$ , then the survival probability is given by

$$P_{\bar{\nu}_e \rightarrow \bar{\nu}_e}(E_\nu, r) = \langle \bar{\nu}_e | \hat{\rho}(E_\nu, r) | \bar{\nu}_e \rangle. \quad (27)$$

We calculate this both numerically by solving the evolution equation given in Eq. (10), and analytically by using the decoupling approximation together with the Landau-Zener jumping probabilities. Note that here we temporarily reintroduce the

neutrino energy  $E_\nu$  into our notation to emphasize the energy dependence of the survival probability.

After that, we consider a mixed ensemble of neutrinos as appropriate for the cooling period of the proto-neutron star. In this case, the initial density operator is in the diagonal form

$$\hat{\rho}(E_\nu, R) = \sum_{\alpha=e,\bar{e},x,\bar{x}} \rho_{\alpha\alpha}(E_\nu, R) |\nu_\alpha\rangle \langle \nu_\alpha|, \quad (28)$$

where  $\rho_{\alpha\alpha}(E_\nu, R)$  is the  $\nu_\alpha$  energy spectrum emitted from the neutrinosphere in arbitrary units. Here,  $\alpha = e, \bar{e}, x, \bar{x}$  and we use  $\nu_{\bar{\alpha}}$  to mean  $\bar{\nu}_\alpha$ . We again calculate the corresponding density operator  $\hat{\rho}(E_\nu, r)$  at  $r$  both numerically and analytically as described above. Corresponding  $\nu_\alpha$  energy spectrum at  $r$  is given by

$$\rho_{\alpha\alpha}(E_\nu, r) = \langle \nu_\alpha | \hat{\rho}(E_\nu, r) | \nu_\alpha \rangle. \quad (29)$$

In both cases (for the pure ensemble of electron antineutrinos and for the mixed ensemble) analytical calculations start by expressing the initial density operator in energy eigenbasis at  $R$  as

$$\hat{\rho}(R) = \sum_{i,j=1}^4 \rho_{ij}(R) |R_i\rangle \langle R_j| \quad (30)$$

with  $\rho_{ij}(R) = \langle R_i | \hat{\rho}(R) | R_j \rangle$  denoting the corresponding components. Here, we again drop the energy dependence from our notation. We emphasize that although Latin indicies are typically used to refer mass basis in the literature, we use them to refer to energy eigenbasis in this paper.

Let us first assume that the adiabaticity condition holds through both resonances. We consider the partially adiabatic evolution in the next two sections. In the adiabatic case, the evolution is completely determined by Eq. (14). The density operator evolves into

$$\hat{\rho}(r) = \sum_{i,j=1}^4 e^{-i \int_R^r (E_i - E_j) dr} \rho_{ij}(R) |r_i\rangle \langle r_j| \quad (31)$$

at a later  $r$ . As the neutrinos reach to the surface of the supernova, the Hamiltonian is reduced to the vacuum term alone and the energy eigenstates reduce to the mass eigenstates. Which energy eigenstate reduces to which mass eigenstate depends on the hierarchy. We have

$$\begin{aligned} |r_1\rangle, |r_2\rangle, |r_3\rangle, |r_4\rangle &\xrightarrow{n\theta \rightarrow 0} |\bar{\nu}_2\rangle, |\nu_2\rangle, |\nu_1\rangle, |\bar{\nu}_1\rangle \text{ in NH,} \\ |r_1\rangle, |r_2\rangle, |r_3\rangle, |r_4\rangle &\xrightarrow{n\theta \rightarrow 0} |\nu_1\rangle, |\bar{\nu}_1\rangle, |\bar{\nu}_2\rangle, |\nu_2\rangle \text{ in IH.} \end{aligned} \quad (32)$$

These are also indicated in Fig. 2.

After that, neutrinos travel a long distance to Earth and during this time they decohere. Decoherence happens because neutrino mass eigenstates travel with different speeds in vacuum and a gap opens up between them over long distances. When neutrino mass eigenstates do not overlap in physical space, they cannot interfere and the flavor oscillations stop [55]. The standard mathematical formulation of neutrino oscillations, which we also use here, is based on the assumption that neutrinos are plain waves with infinite wavepackage size. The formulation of

the decoherence requires the finite size of the wavepackage to be taken into account. In this case, the off diagonal elements of the density matrix in mass basis pick up an exponential term  $e^{-(r/r_{\text{coh}})^2}$  [56]. The coherence length  $r_{\text{coh}}$  depends on the wave package size, which in turn depends on the circumstances of the neutrino's creation. For a physically intuitive discussion, see Section 8 of Ref. [57]. For supernova neutrinos the coherence length can be estimated to be of the order of  $10^6$  km [57, 58]. For this reason, plane wave formulation is a good approximation inside the star. But even for a galactic supernova, neutrinos have to travel several kilo parsecs (about  $10^{17}$  km) to reach Earth. Therefore, one can take  $r \rightarrow \infty$  limit where  $e^{-(r/r_{\text{coh}})^2} \rightarrow 0$ . Therefore the decoherence of neutrinos over long distances can be implemented in practice by removing the off-diagonal elements of the density operator in the mass basis. As a result, in the fully adiabatic case the neutrinos arriving Earth is described by

$$\hat{\rho}(\infty) = \sum_{i=1}^4 \rho_{ii}(R) |r_i\rangle \langle r_i| \quad (33)$$

with  $|r_i\rangle$  given by Eq. (32) according to mass hierarchy. In particular, for the initial pure ensemble of electron antineutrinos given in Eq. (26), one finds

$$\hat{\rho}(\infty) = \sin^2 \theta_B(R) |\nu_1\rangle \langle \nu_1| + \cos^2 \theta_B(R) |\bar{\nu}_1\rangle \langle \bar{\nu}_1|. \quad (34)$$

Here we used Eq. (20) to calculate  $\rho_{ii}(R)$  in terms of the effective mixing angle  $\theta_B(R)$  on the surface of the neutrinosphere. Using the fact that  $\langle \nu_1 | \bar{\nu}_e \rangle = 0$  and  $\langle \bar{\nu}_1 | \bar{\nu}_e \rangle = \cos \theta$ , the survival probability of an initial  $\bar{\nu}_e$  is found from Eq. (27) as

$$P_{\bar{\nu}_e \rightarrow \bar{\nu}_e}(\infty) = \left( \frac{1}{2} + \frac{1}{2} \cos 2\theta_B(R) \right) \cos^2 \theta, \quad (35)$$

which is the standard result. See Ref. [59], for example.

## 5. Zero mixing angle

### 5.1. General treatment

Here and in the next section, we consider the partially adiabatic evolution of neutrinos. In this section we take  $\theta = 0$  which removes the MSW resonance from the picture and allows us to focus on the phase effects between the production point and the partially adiabatic SFP resonance.  $\theta \neq 0$  case is discussed in the next section where additional phase effects from the MSW resonance also enter into the picture.

The adiabaticity of SFP resonance is quantified by [13, 59, 60]

$$\Gamma_B = \left( \frac{(\mu B)^2}{\sqrt{2} G_F \frac{1}{m_n} \left| \frac{dn(r)}{dr} \right| (1 - 2Y_e)} \right)_{\text{res}}, \quad (36)$$

where the subscript ‘‘res’’ indicates that the expression should be calculated at the SFP resonance. The Landau-Zener approximation tells us that the probability of the system to jump between the resonating energy eigenstates  $|r_3\rangle$  and  $|r_4\rangle$  in NH is

$$P_B = e^{-2\pi\Gamma_B}. \quad (37)$$



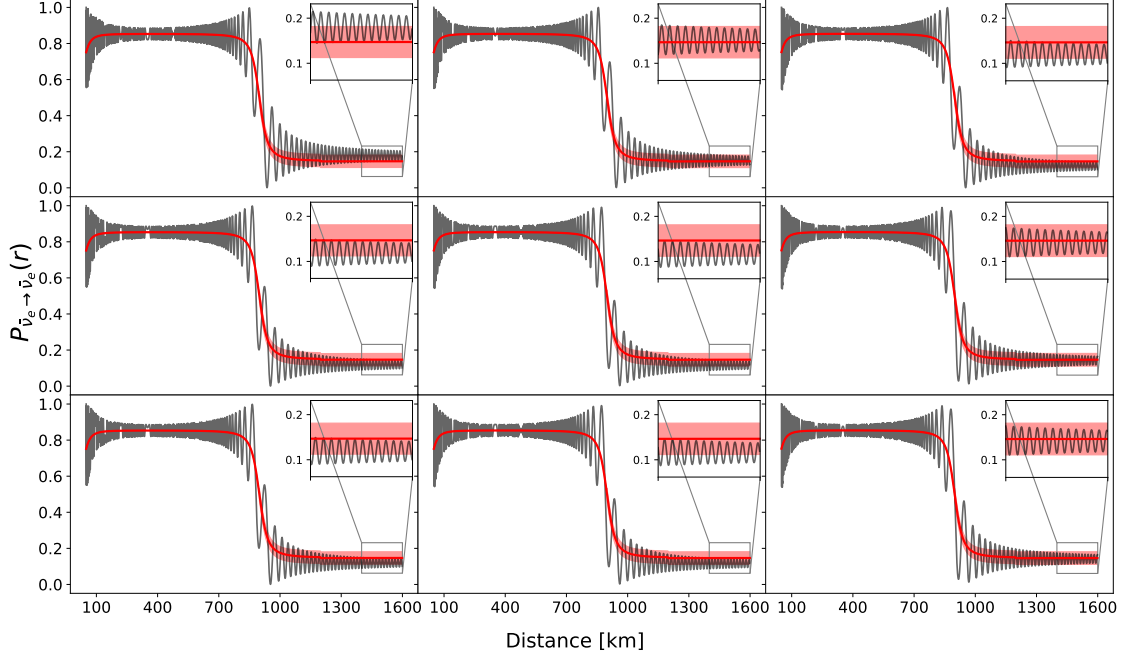


**Figure 4:** The survival probability of a 15 MeV electron antineutrino at 5s post-bounce time for exponentially fitted density distributions under slightly different evolution conditions. The rows correspond to  $R/\text{km} = 49.95, 50.00, 50.05$  and the columns correspond to  $r_{\text{mag}}/\text{km} = 49.95, 50.00, 50.05$ . The grey curves are numerical solutions. The thick red lines (same in every panel) show the theoretically expected mean survival probability in the absence of phase effects (first two lines of Eq. (42)). The red shaded regions (same in every panel) show the theoretically expected range of mean survival probability with the phase effects (the uncertainty from the third line of Eq. (42)). There is a partially adiabatic SFP resonance at 850 km. Before that, the survival probability oscillates around the thick red line indicating SFP without phase effects. After the resonance, the survival probability oscillates around a different mean value in each case which indicates phase effects. However, in each panel the mean survival probability falls in the red shaded region as expected.

Therefore the evolution is described by

$$\begin{pmatrix} |r_3\rangle \\ |r_4\rangle \end{pmatrix} \rightarrow \begin{pmatrix} \sqrt{1-P_B} & -e^{-i\alpha} \sqrt{P_B} \\ e^{-i\alpha} \sqrt{P_B} & \sqrt{1-P_B} \end{pmatrix} \begin{pmatrix} |r_3\rangle \\ |r_4\rangle \end{pmatrix} \quad (38)$$

through the resonance<sup>4</sup>. Here  $\alpha$  is called the Stoke's phase [32, 33]. If  $P_B \approx 0$  then no jumping occurs from one eigenstate to the other which is the adiabatic limit. In this limit the Stoke's phase becomes irrelevant. The Stoke's phase is also irrelevant in the opposite (sudden) limit where  $P_B \approx 1$  because it can be included in the definition of the local eigenstates. But if  $0 < P_B < 1$ , then the Stoke's phase should be included in the calculation. However, as we discuss below, it becomes important only when the state entering the resonance is a combination of the energy eigenstates  $|r_3\rangle$  and  $|r_4\rangle$ .

Neutrinos evolve adiabatically until the SFP resonance point, which we denote by  $r_B$ . Before the resonance, the density operator is given by Eq. (31). After the resonance, it is given

by

$$\begin{aligned} \hat{\rho}(r) &= \rho_{11}(R) |r_1\rangle \langle r_1| + \rho_{22}(R) |r_2\rangle \langle r_2| \\ &+ ((1-P_B)\rho_{33}(R) + P_B\rho_{44}(R)) |r_3\rangle \langle r_3| \\ &+ (P_B\rho_{33}(R) + (1-P_B)\rho_{44}(R)) |r_4\rangle \langle r_4| \\ &+ (e^{i\phi_B} \sqrt{P_B(1-P_B)}\rho_{34}(R) + \text{cc}) (|r_3\rangle \langle r_3| - |r_4\rangle \langle r_4|) \\ &+ (\dots) e^{-i \int_{r_B}^r (E_3 - E_4) dr} |r_3\rangle \langle r_4| + \text{hc} \end{aligned} \quad (39)$$

in accordance with Eq. (38). Here,  $\rho_{ij}(R)$  are the matrix elements of the density operator in the energy eigenbasis at  $R$  defined in Eq. (30). The last line of this result is off-diagonal in the energy eigenbasis and fluctuates very fast around zero. Here hc denotes the hermitian conjugate of this last term. The coefficients in the last line are not shown explicitly because they will eventually die due to decoherence as explained in the previous section. For this reason, we focus on the first four lines which are diagonal. These terms change smoothly as the energy eigenstates slowly vary with external conditions and determine the survival probability over long distances. First three lines among them represent the ‘‘classical’’ outcome (i.e., no phase effects) in the sense that they depend only on the Landau-Zener

<sup>4</sup>Strictly speaking, Eqs. (36)-(38) assume that the magnetic field is constant around the resonance region. This is not the case for our magnetic field profile. But the comparison between our numerical and analytical results indicate that this variation can be ignored here.

transition probabilities. In contrast, the fourth line is an ‘‘interference’’ term (i.e., phase effects) which depends on the relative phase between  $|r_3\rangle$  and  $|r_4\rangle$  acquired from the production point  $R$  to the SFP resonance point  $r_B$ , as well as the Stoke’s phase  $\alpha$ . The sum of these two phases denoted by  $\phi_B$  in the fourth line of Eq. (39), i.e.,

$$\phi_B = - \int_R^{r_B} (E_3(r) - E_4(r))dr + \alpha, \quad (40)$$

is precisely what creates the SFP phase effect. Notice that this is a fixed phase, i.e., it does not lead to oscillations. Instead, it contains the cumulative effects of the individual evolutions energy eigenstate components from the production point  $R$  to the SFP resonance point  $r_B$ , giving rise to an interference between them. Naturally, this occurs only when the terms that multiply it in the fourth line are different from zero, i.e., when  $\rho_{34}(R) \neq 0$  and  $0 < P_B < 1$ . If these conditions are satisfied then the interference term affects the survival probabilities in  $r \rightarrow \infty$  limit and creates the SFP phase effect. The phase  $\phi_B$  depends sensitively on the details of how the neutrino undergoes from production point to the resonance point. But, as explained at the beginning of Section III, neutrinos represented by  $\hat{\rho}(r)$  would be subject to slightly different evolution conditions. In practice  $\phi_B$  will be different for every neutrino and therefore it should be treated as an *uncertainty* by taking  $-\pi \leq \phi_B < \pi$ .

The emergence of the SFP phase effect due to the phase given in Eq. (40) and its sensitive dependence on external conditions are demonstrated in Fig. 4. This figure shows the survival probability of a 15 MeV electron antineutrino as a function of distance under slightly different evolution conditions. We use the exponentially fitted density distribution at 5s post-bounce time, but change the external conditions by slightly varying the radius of the neutrinosphere  $R$  and the distance scale  $r_{\text{mag}}$  with which the magnetic field decreases. The rows correspond to  $R/\text{km} = 49.95, 50.00, 50.05$  and the columns correspond to  $r_{\text{mag}}/\text{km} = 49.95, 50.00, 50.05$ . The variation of  $R$  mimics possible decoupling at slightly different radii from the neutron star, or traveling slightly different distances due to being emitted at different angles. The variation of  $r_{\text{mag}}$  mimics experiencing slightly different magnetic field profiles due to changing conditions or traveling at different angles with it.

The grey lines in Fig. 4 show the solutions obtained by numerically solving the evolution equation given in Eq. (10). The thick red lines show the theoretically expected average survival probabilities in the absence of SFP phase effects. The fact that the grey lines are oscillating perfectly around the thick red lines before 850 km tells us that there are no phase effects in this region. This is to be expected because, although the neutrino fulfills the first condition for the emergence of the phase effects mentioned in the Introduction (see below), the second condition is satisfied only when it goes through the partially adiabatic SFP resonance which sits at 850 km. The red shaded regions show the range of the theoretically expected average survival probability with the phase effects taken into account by setting  $-\pi \leq \phi_B < \pi$ . The fact that the grey lines start oscillating around averages which fall into the red shaded regions instead of oscillating around the thick red lines after 850 km shows that

the SFP phase effect has emerged. This can be better observed in the insets where the low density parts are enlarged.

It is useful to mention how we obtain the theoretically expected survival probabilities (thick red line and the red shaded regions) in Fig. 4. For this, we start from a pure ensemble as in Eq. (26) and use Eq. (20) to obtain non-zero matrix elements of the density matrix in energy eigenbasis:

$$\begin{aligned} \rho_{33}(R) &= \sin^2\theta_B(R), & \rho_{44}(R) &= \cos^2\theta_B(R), \\ \rho_{34}(R) &= \rho_{43}(R) = \sin\theta_B(R)\cos\theta_B(R). \end{aligned} \quad (41)$$

The second line of the above equation is what tells us that the neutrino is already in a superposition of energy eigenstates when it is born. Eqs. (27), (31) and (39) then yield the following formula for survival probability:

$$\begin{aligned} P_{\bar{\nu}_e \rightarrow \bar{\nu}_e}(r) &= \left[ (1 - P_B)\sin^2\theta_B(R) + P_B\cos^2\theta_B(R) \right] |\langle r_3 | \bar{\nu}_e \rangle|^2 \\ &+ \left[ P_B\sin^2\theta_B(R) + (1 - P_B)\cos^2\theta_B(R) \right] |\langle r_4 | \bar{\nu}_e \rangle|^2 \\ &\pm \sqrt{P_B(1 - P_B)} \sin 2\theta_B(R) (|\langle r_3 | \bar{\nu}_e \rangle|^2 - |\langle r_4 | \bar{\nu}_e \rangle|^2) \\ &+ \text{terms oscillating around zero.} \end{aligned} \quad (42)$$

This formula is valid with  $P_B = 0$  before the SFP resonance at 850 km, and with  $P_B$  given by Eq. (37) after it. The last line contains fast oscillations around zero which we do not explicitly write down. If we disregard these fast oscillations, what remains is the mean survival probability described by the first three lines. The first two lines come from the classical probability (i.e., no phase effects) part of Eq. (39) and give us the thick red line in Fig. 4. The third line comes from interference (i.e., phase effect) term of Eq. (39). Varying the phase within the full range as explained above brings the  $\pm$  sign and gives us the red shaded uncertainty region around the thick red line. Note that the small variations of  $R$  and  $r_{\text{mag}}$  mentioned above are almost irrelevant for the values of  $P_B$  and  $\theta_B(R)$ . For this reason, the thick red line and the red shaded regions are identical in all the panels of Fig. 4

## 5.2. At $r \rightarrow \infty$ limit

The decoherence over long distances can be implemented by discarding the off-diagonal terms of the density operator given in Eq. (39), which removes all oscillations. Using Eq. (32) for NH we find the following analytical expression for the density operator in  $r \rightarrow \infty$  limit:

$$\begin{aligned} \hat{\rho}(\infty) &= \rho_{11}(R) |\bar{\nu}_2\rangle \langle \bar{\nu}_2| + \rho_{22}(R) |\nu_2\rangle \langle \nu_2| \\ &+ ((1 - P_B)\rho_{33}(R) + P_B\rho_{44}(R)) |\nu_1\rangle \langle \nu_1| \\ &+ (P_B\rho_{33}(R) + (1 - P_B)\rho_{44}(R)) |\bar{\nu}_1\rangle \langle \bar{\nu}_1| \\ &\pm 2\sqrt{P_B(1 - P_B)}\rho_{34}(R) (|\nu_1\rangle \langle \nu_1| - |\bar{\nu}_1\rangle \langle \bar{\nu}_1|). \end{aligned} \quad (43)$$

In particular, we find the analytical expression for the limiting survival probability of an initial  $\bar{\nu}_e$  from Eqs. (41) and (43) as

$$\begin{aligned} P_{\bar{\nu}_e \rightarrow \bar{\nu}_e}(\infty) &= (P_B \sin^2\theta_B(R) + (1 - P_B) \cos^2\theta_B(R)) \\ &\pm \sqrt{P_B(1 - P_B)} \sin 2\theta_B(R). \end{aligned} \quad (44)$$

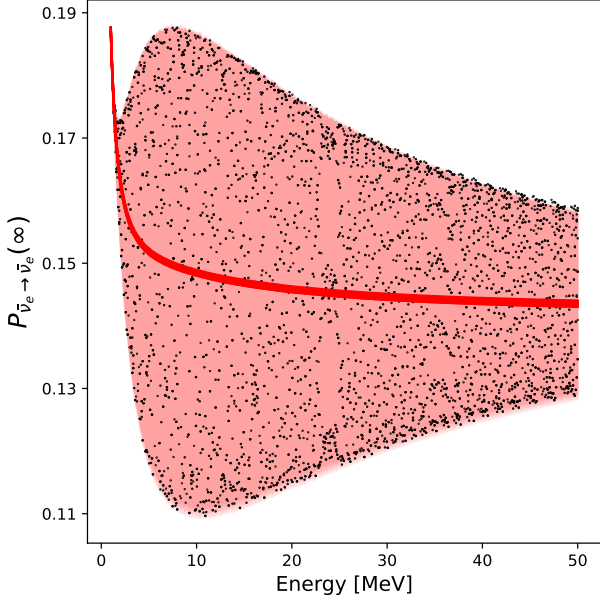


**Figure 5:** The survival probability of a  $\bar{\nu}_e$  for the exponentially fitted density distribution at  $t = 5$  s in  $r \rightarrow \infty$  limit as a function of energy. The thick red line is the classical probability result obtained from the first line of Eq. (44). The red shaded region is the uncertainty obtained from the second line of the same equation. For each neutrino energy, 9 numerical simulations are carried out with the same  $R$  and  $r_{\text{mag}}$  parameters as in Fig. 4. The black dots represent the limiting survival probabilities obtained from these simulations as described in the text.

Here we also use Eq. (32) and the fact that  $\langle \nu_1 | \bar{\nu}_e \rangle = 0$  and  $\langle \bar{\nu}_1 | \bar{\nu}_e \rangle = 1$  since the mixing angle is taken to be zero.

In our numerical simulations the oscillations do not die over long distances because our equation of motion given in Eq. (10) does not take decoherence into account. We approach this situation as follows: First, we run the simulation until the density is low enough to be considered vacuum. This happens somewhere between a few to several thousand kilometers depending on the post-bounce time and the neutrino energy. Once we observe that the survival probability starts to oscillate steadily around a fixed average value, we stop the simulation and remove the off diagonal elements of the resulting density operator in mass basis. Doing this brings the survival probability to the average value around which the numerical result steadily oscillates in vacuum.

We show the  $\bar{\nu}_e$  survival probability at  $r \rightarrow \infty$  limit as a function of energy for the exponentially fitted density distribution at  $t = 5$  s in Fig. 5. The solid red line is the classical probability result obtained from the first line of Eq. (44) and the red shaded region is the uncertainty from the second line of the same equation. Each black dot in this figure represents a numerical run. To obtain them, we divide the energy range into 250 bins, and run 9 simulations for each bin with the same  $R$  and  $r_{\text{mag}}$  parameters as those in Fig. 4. But unlike in Fig. 4 where we stop at 1600 km, in Fig. 5 we continue the simulations until the vacuum is reached and obtain the numerical value of the

limiting survival probability as described above. The result of each run is shown with a black dot in Fig. 5. Note that, if we used the same set of external conditions for each energy bin, the survival probability would display fast oscillations with energy. But, since even those neutrinos with the same energy are likely to experience slightly different external conditions as discussed above, we choose this approach and present our results as scattering plots as in Ref. [21]. A total of 2250 numerical simulations were carried out to generate this figure and using exponential fits for the density profiles substantially reduces the total running time. Fig. 5 tells us that the survival probability of an initial  $\bar{\nu}_e$  can change by as much as %30 depending on the energy under the adopted conditions. But in each numerical run the limiting survival probability always falls into the uncertainty range predicted by Eq. (44).

## 6. Non-zero mixing angle

When the mixing angle is not zero, neutrinos go through both SFP and MSW resonances. For  $Y_e > 1/3$ , which is most often the case, MSW resonance takes place after the SFP resonance. The adiabaticity of the MSW resonance is quantified by the parameter

$$\Gamma_M = \left( \frac{(\frac{\delta m^2}{2E} \sin 2\theta)^2}{\sqrt{2} G_F \frac{1}{m_n} \left| \frac{dn(r)}{dr} \right| Y_e} \right)_{\text{res}}, \quad (45)$$

where the subscript “res” indicates that the expression should be calculated at the resonance. The Landau-Zener approximation tells us that the jumping probability between the resonating energy eigenstates  $|r_2\rangle$  and  $|r_3\rangle$  in NH is

$$P_M = e^{-2\pi\Gamma_M}. \quad (46)$$

Therefore the evolution through the MSW resonance is described by

$$\begin{pmatrix} |r_2\rangle \\ |r_3\rangle \end{pmatrix} \rightarrow \begin{pmatrix} \sqrt{1-P_M} & -e^{-i\beta} \sqrt{P_M} \\ e^{-i\beta} \sqrt{P_M} & \sqrt{1-P_M} \end{pmatrix} \begin{pmatrix} |r_2\rangle \\ |r_3\rangle \end{pmatrix}, \quad (47)$$

where  $\beta$  is the Stoke’s phase. For a completely adiabatic ( $P_M = 0$ ) or completely nonadiabatic ( $P_M = 1$ ) resonance the Stoke’s phase is unimportant. But in partially adiabatic case with  $0 < P_M < 1$ , it should be taken into account.

In between the SFP and MSW resonances the density operator is given by Eq. (39). After the MSW resonance Eq. (47) must also be applied to it which results in a complicated generic form. Here we do not reproduce the full result because it is not relevant for our purposes. Instead, we give its  $r \rightarrow \infty$  limit which we obtain by removing its off-diagonal components and

using Eq. (32). The result is

$$\begin{aligned}
\hat{\rho}(\infty) = & \rho_{11}(R) |\bar{\nu}_2\rangle \langle \bar{\nu}_2| \\
& + [(1-P_M)\rho_{22}(R) + P_M((1-P_B)\rho_{33}(R) + P_B\rho_{44}(R))] \\
& \quad \times |\nu_2\rangle \langle \nu_2| \\
& + [P_M\rho_{22}(R) + (1-P_M)((1-P_B)\rho_{33}(R) + P_B\rho_{44}(R))] \\
& \quad \times |\nu_1\rangle \langle \nu_1| \\
& + [P_B\rho_{33}(R) + (1-P_B)\rho_{44}(R)] |\bar{\nu}_1\rangle \langle \bar{\nu}_1| \\
& \pm 2\sqrt{(1-P_B)P_B} |\rho_{34}(R)| \\
& \quad \times [(1-P_M)|\nu_1\rangle \langle \nu_1| + P_M|\nu_2\rangle \langle \nu_2| - |\bar{\nu}_1\rangle \langle \bar{\nu}_1|] \\
& \pm 2\sqrt{(1-P_M)P_M} [\sqrt{P_B}|\rho_{24}(R)| + \sqrt{1-P_B}|\rho_{23}(R)|] \\
& \quad \times (|\nu_2\rangle \langle \nu_2| - |\nu_1\rangle \langle \nu_1|) \quad (48)
\end{aligned}$$

The first four lines of this equation involve only the probabilities and represent the classical result. The last two lines give the uncertainty due to the phases. In addition to the one given in Eq. (40), other phases also enter the result: These are the relative phases acquired by  $|r_3\rangle$  and by  $|r_4\rangle$  with respect to  $|r_2\rangle$  from production to the SFP resonance, the relative phase between  $|r_2\rangle$  and  $|r_3\rangle$  from the SFP resonance to the MSW resonance, and the Stoke's phase  $\beta$  associated with the MSW resonance. These phases show up in combinations so that there are only two uncertainty terms in the final result. Note that Eq. (48) reduces to Eq. (43) when the MSW resonance is fully adiabatic, i.e., when  $P_M = 0$ . In particular, for an initial electron antineutrino, the limiting survival probability can be calculated by using Eq. (41) and the relations  $\langle \nu_1 | \bar{\nu}_e \rangle = 0$  and  $\langle \bar{\nu}_1 | \bar{\nu}_e \rangle = \cos \theta$ . The result is

$$\begin{aligned}
P_{\bar{\nu}_e \rightarrow \bar{\nu}_e}(\infty) = & (P_B \sin^2 \theta_B(R) + (1-P_B) \cos^2 \theta_B(R)) \cos^2 \theta \\
& \pm \sqrt{P_B(1-P_B)} \sin 2\theta_B(R) \cos^2 \theta, \quad (49)
\end{aligned}$$

which reduces to Eq. (44) when  $\theta = 0$ . This formula does not contain  $P_M$ . This is expected because we focus on NH in which case antineutrinos do not experience the MSW resonance. However, from Fig. 2 we see that the component of the initial  $\bar{\nu}_e$  which turns into  $\nu_x$  in SFP resonance later experiences MSW resonance, and here it can partially or fully turn into  $\nu_e$ . Therefore we expect the  $\bar{\nu}_e \rightarrow \nu_e$  transition probability to involve both  $P_B$  and  $P_M$ . Substituting Eq. (41) into Eq. (48) and taking the matrix element  $\langle \nu_e | \hat{\rho}(\infty) | \nu_e \rangle$  leads to the result

$$\begin{aligned}
P_{\bar{\nu}_e \rightarrow \nu_e}(\infty) = & (P_B \sin^2 \theta_B(R) + (1-P_B) \cos^2 \theta_B(R)) \\
& \quad \times ((1-P_M) \cos^2 \theta + P_M \sin^2 \theta) \\
& \pm \sqrt{P_B(1-P_B)} \sin 2\theta_B(R) \cos^2 \theta \quad (50)
\end{aligned}$$

Fig. 6 shows the survival probability of an electron antineutrino at  $r \rightarrow \infty$  limit as a function of neutrino energy for  $\mu = 1 \times 10^{-16} \mu_B$  and for the exponentially fitted density distributions at different post-bounce times. The solid red lines show the average survival probability and the red shaded areas show the uncertainty region, both calculated from Eq. (49). The

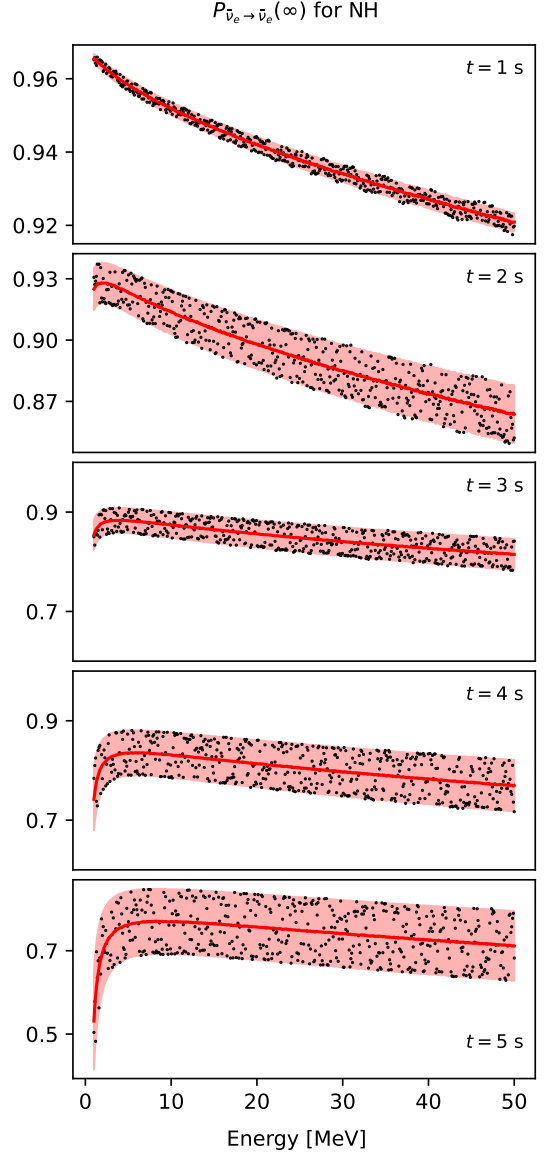


**Figure 6:** The electron antineutrino survival probability at  $r \rightarrow \infty$  limit as a function of energy for  $\mu = 1 \times 10^{-16} \mu_B$  and for exponentially fitted density distributions. The panels show the post-bounce times  $t = 1, 2, 3, 4, 5$  s from top to bottom. The solid red lines and the red shaded regions respectively show the average survival probability and the associated uncertainty calculated from Eq. (49). The black dots are the limiting survival probabilities obtained from numerical solutions under slightly different and randomly chosen conditions as described in the text.

black dots represent the results obtained by numerically solving Eq. (10) under very similar but slightly different conditions as described in the context of Fig. 5. But this time, for each neutrino energy we solve the evolution equation three times. In each run we choose both  $R$  and  $r_{\text{mag}}$  randomly and independently in the interval (49.95 km, 50.05 km). As can be seen, all numerical results are within the uncertainty bounds predicted by Eq. (49).

Fig. 7 shows the same results for  $\mu = 5 \times 10^{-16} \mu_B$ . Here we

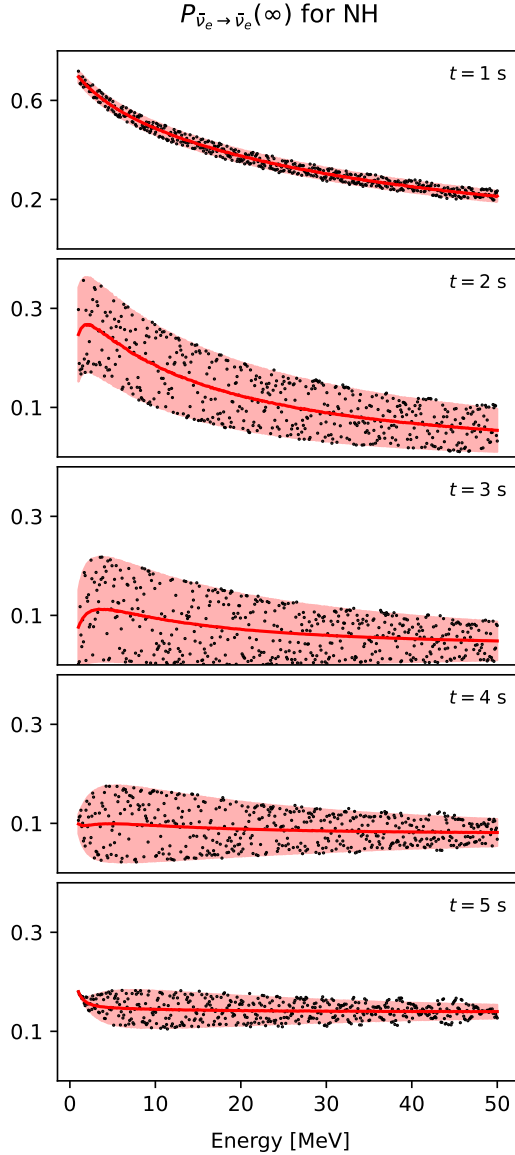


**Figure 7:** Same as Fig. 6, but for  $\mu = 5 \times 10^{-16} \mu_B$ .

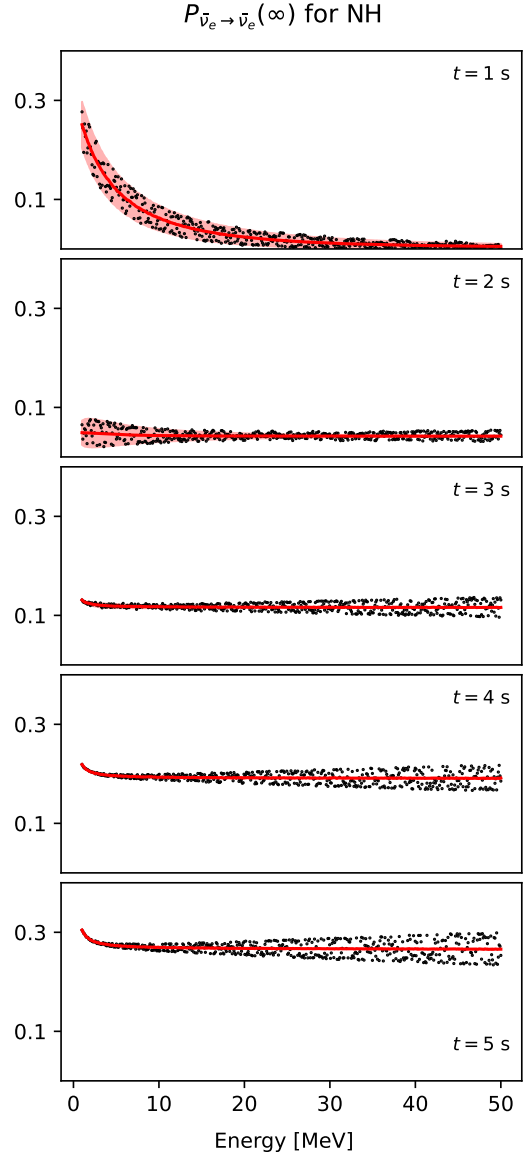


**Figure 8:** Same as Fig. 6, but for  $\mu = 10 \times 10^{-16} \mu_B$ .

see a few differences from Fig. 6. First, the survival probability of  $\bar{\nu}_e$  drops to significantly lower values. This is because for larger  $\mu$  the SFP resonance is more adiabatic according to Eq. (36), which makes the  $\bar{\nu}_e \rightarrow \nu_x$  transition more efficient. Second, some numerical results are slightly out of the analytical uncertainty region at late times. This is because our analytical treatment is based on the decoupling approximation in which SFP and MSW resonances can be treated as two separate two-level problems within the Landau-Zener formalism. Due to the widening of SFP resonance examined in Section III, this approach eventually fails at late times, especially for larger  $\mu B$  values.

Fig. 8 shows our results for an even larger magnetic moment of  $\mu = 10 \times 10^{-16} \mu_B$ . In this figure two things can be observed: First, the uncertainty predicted by our analytical approach becomes zero at late post-bounce times. This is because

the SFP moves inside and happens under a stronger magnetic field. Eventually, the  $\mu B$  value at the SFP resonance becomes large enough to render it completely adiabatic at late times. MSW resonance is also adiabatic for the model that we work with. In this case, the predicted uncertainty vanishes. In other words since both resonances are adiabatic analytical approach suggests that there is no phase effect. However, (and this is the second observation) we see that the numerical results still indicate the presence of a phase effect. This is due to the failure of the decoupling scheme. As discussed in Section III, the SFP resonance becomes wider at late post-bounce times. This widening effect is even more pronounced for large  $\mu$ . We conclude that if SFP and MSW resonances overlap, the phase effect may still be there even when individual resonances seem to be adiabatic from a straightforward application of the Landau-Zener approach.



## 7. Observability of SFP Phase Effect

Phase effects cause the neutrino survival and transition probabilities to randomly fluctuate around an average value. From an observational point of view, each dot in Figs. 6 - 8 may be thought as a possible neutrino interacting at the detector. If many neutrinos are captured in a given energy bin in a given time interval, their combined effect would average out this fluctuation. In other words, although neutrinos emitted in a small time and energy interval arrive at the detector in different final states, the net effect would be the same as if the detector is responding to a smooth neutrino signal. In this case, it is appropriate to ignore the phase effects from the beginning as is often the practice in the literature. But, if only a few neutrinos can be captured in each energy bin, then averaging cannot completely remove the randomization. In this case, the detector would in principle be responding to an irregular neutrino signal. However, this irregularity can still get lost if the detector cannot resolve it. In what follows, we first demonstrate SFP phase effect in a realistic scenario, and then talk about its observability.

We start with the mixed ensemble of neutrinos as described in Eq. (28). We take the initial energy distributions to be of Fermi-Dirac type<sup>5</sup> and evolve it using the realistic density profiles, i.e., the solid lines shown in Fig. 1. As discussed just below Eq. (8), the realistic density profiles decrease more slowly than the analytical fits and consequently the resonances take place in outer regions where the magnetic field is weaker. As a result, magnetic moments of the order of  $10^{-16}\mu_B$  used in illustrative discussion create smaller amounts of smearing with realistic density profiles. However, a stronger magnetic moment can offset this effect and create a larger smearing.

Fig. 9 shows our results for  $\mu = 5 \times 10^{-15}\mu_B$  with realistic density profiles for a supernova at 10 kpc distance from Earth with a total energy of  $3 \times 10^{53}$  ergs. The energy is shared equally among all six flavors (see, e.g., Ref. [21]) while each flavor has a different thermalization with  $kT_{\nu_e} = 3.0$  MeV,  $kT_{\bar{\nu}_e} = 5.0$  MeV, and  $kT_{\nu_x} = kT_{\bar{\nu}_x} = 7.0$  MeV where  $T_{\nu_\alpha}$  denotes the temperature for the  $\nu_\alpha$  flavor and  $k$  denotes the Boltzmann constant. The panels in this figure show post-bounce times  $t = 1, 3, 5$  s from top to bottom. The dashed lines show the energy distribution of neutrino fluxes on the proto-neutron star surface with red, black, blue, and green colors respectively corresponding to  $\nu_e, \nu_x, \bar{\nu}_e,$  and  $\bar{\nu}_x$  flavors. We use arbitrary units so as to be able to compare these fluxes with the ones reaching Earth. The dots represent the results of our numerical simulations. We obtain them by solving the evolution described by Eq. (10) for the realistic density profiles up until the vacuum and then by applying decoherence in  $r \rightarrow \infty$  limit. As before, we do this three times for each energy bin by choosing  $R$  and  $r_{\text{mag}}$  randomly and independently in the interval (49.95 km, 50.05 km). If a single set of parameters were used instead of randomization, the resulting energy spectra would rapidly oscillate around an average

<sup>5</sup>If the neutrino magnetic moment is large, then the neutrino spectra emerging from the proto-neutron star may be different from Fermi-Dirac type due to neutrino electromagnetic interactions inside the core. See, for example, Refs. [61–63]. We do not consider this effect here.

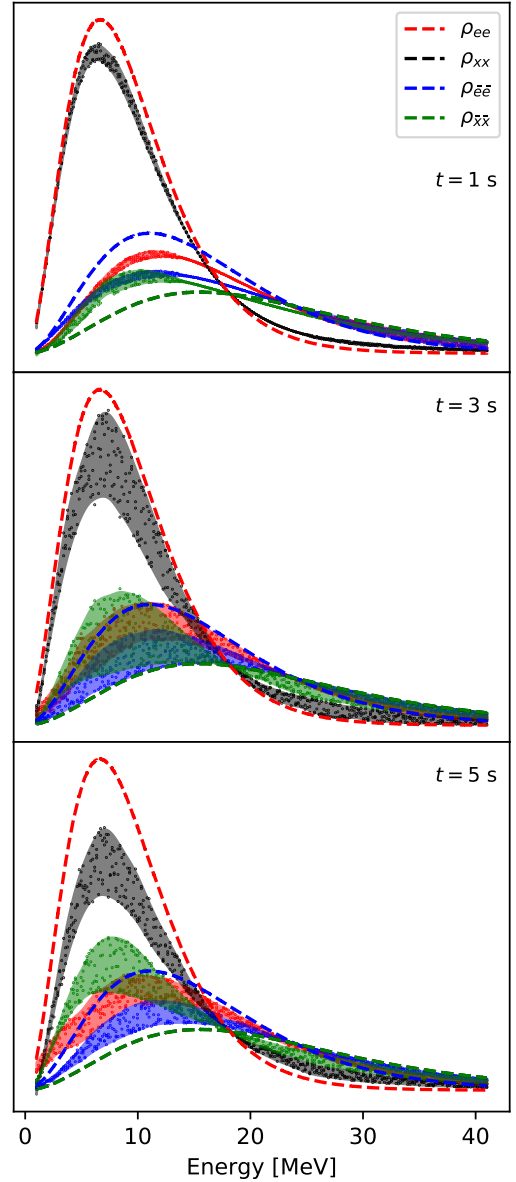


**Figure 9:** Smearing of the supernova neutrino flux at Earth for  $\mu = 5 \times 10^{-15}\mu_B$  in arbitrary units. The panels correspond to  $t = 1, 3, 5$  s from top to bottom. The dashed lines show initial neutrino fluxes with Fermi-Dirac type distributions. The dots in the same color coding show the numerical results obtained by introducing small random variations for each energy bin as described in the text. We use realistic density profiles shown with the solid lines in Fig. 1. The shaded areas do not represent the analytically expected uncertainty as in previous figures, but serve to indicate the distribution of numerical results.

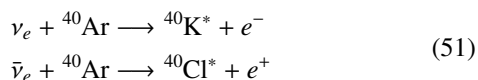
distribution. However, as discussed before, it is more realistic to assume that neutrinos would experience slightly different external conditions due to their direction of travel, for instance. Unlike in previous figures, the shaded regions in Fig. 9 do not represent analytically calculated uncertainty ranges because we are using realistic density profiles rather than their analytical fits. Instead, these regions are drawn by hand to guide the eye about the spreading of the points. Color coding for the dots and

the shaded regions are the same as those for the initial distributions. Note that, we calculate up to 100 MeV neutrino energy but we show the spectra only up to 40 MeV in Fig. 9 for clarity. For larger energies, the colored regions overlap with each other. However, high energy neutrinos are important for the detector response. For this reason energies up to 100 MeV will be included in event rate calculations below.

Fig. 9 tells us that the phase effect makes little impact at the early time of  $t = 1$  s. This is expected because the matter density at the neutrinosphere is relatively high and flavor eigenstates are close to energy eigenstates. However, at later times decreasing density near the neutrinosphere drives the initial energy eigenstates away from flavor eigenstates and cause neutrinos to experience a more pronounced SFP phase effect. Colored regions are particularly wide around 5 – 15 MeV. This is due to the fact that the original distributions differ most from each other in this energy region and therefore any uncertainties in the survival and transition probabilities make the strongest impact here.

What is the significance of Fig. 9 from an observational point of view? The answer is that the colored regions are the zones in which the energy distributions of the neutrinos *captured by the detector* can possibly lie. As discussed above, if the detector captures many neutrinos in each energy bin, then the randomization will be removed through averaging and the energy distributions will be smooth lines centered inside each colored region. The result would be as if there is no phase effect. But, if a relatively low number of neutrinos are captured, then the distributions would be randomized inside the colored regions. The weaker the signal, the more randomized a distribution the detector will be responding to. A supernova may fall into the second category at late post-bounce times. A typical next generation neutrino detector such as DUNE or Hyper Kamiokande is expected to capture a few thousand neutrinos from a galactic core collapse supernova. But most of them will be detected in the first few seconds after the core bounce. The neutrino luminosity of a supernova decreases approximately as  $\exp(-t/3 \text{ s})$ . For this reason, the detection rate around  $t = 5$  s would drop to a few hundred per second. At the same time our results indicate that the SFP phase effect becomes prominent in amplitude a few seconds after the core bounce. Therefore, if the SFP phase effect is detectable at all, it is reasonable to assume that it will appear at late post-bounce times. In what follows, we investigate the prospect of observing the SFP phase effect with DUNE far detector for the example provided in Fig. 9 at  $t = 5$  s.

DUNE is a liquid scintillator detector currently under construction and it can detect neutrinos in one of the following channels [64]:



For these reactions, the observables are the outgoing leptons together with the decay line of the final excited nuclei. All types of neutrinos can also scatter from both Ar nuclei and electrons, but we do not consider these channels here. Scattering from Ar nuclei proceeds through neutral current interactions alone

and does not distinguish between different neutrino degrees of freedom. As a result, it is insensitive to flavor transformations. Scattering from electrons in principle distinguishes  $\nu_e$  and  $\bar{\nu}_e$  which have larger cross sections than other flavors, but we find that this is not enough to resolve the phase effects.

In Fig. 10, we show the rates of the Ar reaction channels obtained with the SNOwGLoBES [65–67] event rate calculator for three different values of neutrino magnetic moment ( $\mu = 0$ ,  $\mu = 5 \times 10^{-16} \mu_B$ , and  $\mu = 5 \times 10^{-15} \mu_B$  from top to bottom) at three different post-bounce times ( $t = 1, 3, 5$  s from left to right). To obtain the event rates for  $\mu = 5 \times 10^{-15} \mu_B$ , we randomly choose one dot for each flavor per 0.5 MeV from the panels of Fig. 9 (this time we use our full energy range up to 100 MeV) and feed the resulting irregular neutrino spectra into the event rate calculator. For other  $\mu$  values, we calculate similarly. The upper panels show the resulting interaction rates as functions of the neutrino energy assuming that it can be perfectly reconstructed, i.e., before the finite detector energy resolution is incorporated. As expected, the resulting event rates randomly fluctuate. The fluctuations that we observe for  $\mu = 0$  are due to the ordinary phase effect associated with the MSW resonances. Ordinary phase effect can appear only at late times because it requires the presence of two MSW resonances which, as can be seen in Fig. 1, happens only when the reverse shock creates a dip in density profile. This tells us that, the fluctuations that appear at earlier times for  $\mu \neq 0$  are due to SFP phase effects. At later times, ordinary and SFP phase effects are intertwined. According to Fig. 9 for  $\mu = 5 \times 10^{-15} \mu_B$ , SFP phase effect smearing is smaller at  $t = 1$  s in comparison to  $t = 3$  s, but in the corresponding (i.e., the last) row of Fig. 10, we observe larger event rate fluctuations at  $t = 1$  s than at  $t = 3$  s. This is due to the fact that neutrino flux is stronger at earlier times which gives rise to more events at the detector. Also note that in Fig. 10 event rate fluctuations are observed only for energies higher than about 25 MeV despite the fact that Fig. 9 shows SFP phase effect smearing in lower energies as well. This is due to the decrease of neutrino cross sections with energy. The lower panels of Fig. 10 show the same event rates as a functions of detected lepton energy after incorporating the finite detector energy resolution<sup>6</sup>. This process involves folding the event rates with the detector energy resolution function, which is a Gaussian with energy dependent standard deviation given by  $\sigma(E) = E \left( (0.11/\sqrt{E/\text{MeV}})^2 + (0.02)^2 \right)^{1/2}$  for an argon detector [67, 68]. We assume 100% detection efficiency. The fact that no fluctuations are observed in the lower panels tells us that, for the supernova model that we employ and the parameters that we use, the SFP phase effect is washed out in the final lepton spectra. Although SFP phase effects are washed out, SFP itself still makes an impact on the observed event rates. This can be seen by comparing the first row of Fig. 10 ( $\mu = 0$ ) with its second and third rows ( $\mu \neq 0$ ). For all post-bounce seconds, a decrease of electron events and a slight enhancement of positron events can be observed for non-zero magnetic moment.

<sup>6</sup>This is called detector energy smearing in the literature, but we avoid using this term since we use the word smearing to describe the widening of neutrino energy spectra due to the phase effects.



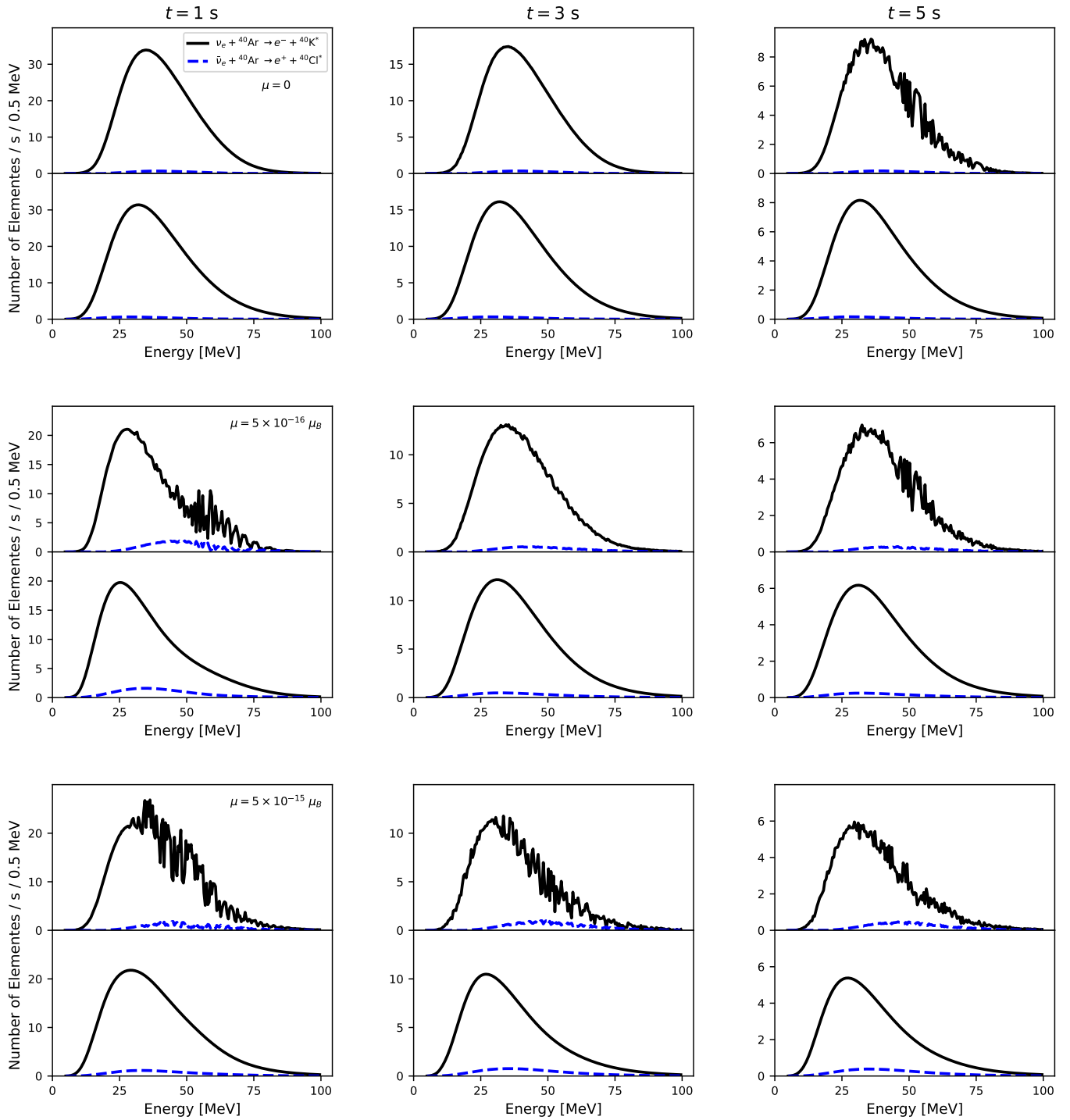


**Figure 10:** Reaction rates on Ar nuclei in DUNE for  $\mu = 0$ ,  $\mu = 5 \times 10^{-16} \mu_B$ , and  $\mu = 5 \times 10^{-15} \mu_B$  (from top to bottom) at  $t = 1, 3, 5$  s post-bounce time (from left to right) for the same model as in Fig. 9. In each plot, upper panels show the interaction rates as functions of neutrino energy, assuming that it can be perfectly reconstructed (i.e., perfect energy resolution). Lower panels show the same event rates as functions of detected lepton energy after incorporating detector energy resolution as described in the text.

## 8. Discussion and Conclusions

In this paper we examined the phase effect caused by neutrino magnetic moment in a core collapse supernova. We assumed that neutrinos are Majorana particles and have a magnetic moment larger than the Standard Model prediction. The large magnetic moment shifts the energy eigenstates away from the flavor eigenstates at the center of the supernova so that each neutrino is emitted as a superposition of energy eigenstates. We showed that the relative phases developed by these energy eigenstates create a phase effect (i) if there is a single partially adiabatic SFP resonance, or (ii) if there are overlapping SFP and MSW resonances. We argued that this distinguishes SFP phase effect from the ordinary phase effect because the latter is manifested only when there are two partially adiabatic MSW resonances.

We approached the problem both analytically and numerically. Our analytical approach is based on the assumption of complete decoupling between SFP and MSW resonances and is applicable only to case (i) above. This approach revealed that the size of the effect does not simply grow with increasing  $\mu B$ . Instead, it depends on an interplay between two factors: The first factor is how far the initial neutrino is from being a pure energy eigenstate and the second factor is how far the resonances are from being completely adiabatic or completely nonadiabatic. Increasing  $\mu B$  initially enhances the SFP phase effect due to the first factor, but increasing  $\mu B$  further suppresses it by making SFP resonance adiabatic.

Our numerical studies revealed that this simple analytical picture can break down at late post-bounce times because SFP and MSW resonances start to overlap. SFP resonance is not universal in the sense that its width in density scale depends on its physical location. At late post-bounce times both resonances physically move inward but the SFP resonance also becomes wider in density scale. Eventually the two resonances start to overlap and the analytical formulation based on the assumption of decoupled resonances collapses. We showed that when the overlap happens, SFP phase effect is present even if SFP and MSW resonances appear to be completely adiabatic from a naive application of the Landau-Zener approach. Figs. 7 and 8 demonstrate this effect at late post-bounce times. This is another aspect that distinguishes SFP phase effect from the ordinary phase effect which involves universal MSW resonances.

To discuss and illustrate these details, we first used simple exponential fits for supernova density profiles at different times. These profiles included one SFP and one MSW resonances. For a realistic density distribution some neutrinos go through more resonances (see Fig. 1), but these additional resonances can only increase the SFP phase effect. This is because once the neutrino is produced, its energy eigenstate components accumulate relative phases by evolving independently. If the additional resonances are partially adiabatic, then they further mix the energy eigenstates and increase the uncertainties. If they are not, then the uncertainties remain the same. Also, the realistic density profile pushes the resonances to the outer regions where the magnetic field is weaker which causes the SFP phase effect to appear for larger neutrino magnetic moments.

Our results for a realistic density distribution and a propagating shock wave demonstrate that those neutrinos with the same energy and the same initial state arrive at the detector with randomized final states due to the SFP phase effect. We argued that observing many neutrinos in an energy bin would average out and effectively remove this randomization, but observing only a few neutrinos would not. As a result, the detector may respond to a somewhat irregular or randomized neutrino signal. We carried out a sample analysis for the capture reactions in Ar nuclei in DUNE. Our analysis showed that, before the finite energy resolution of the detector is taken into account, event rate fluctuations due to the SFP phase effect appear earlier than those due to the ordinary phase effect. Event rate fluctuations also appear only for those neutrinos with energy larger than about 25 MeV, despite the presence of a sizable SFP phase effect below this energy. When the finite energy resolution of the detector is taken into account, however, all fluctuations are erased in the energy spectrum of the observed charged leptons.

There are some aspects of the problem which are left unexplored. For example, the electron fraction is taken to be constant at  $Y_e = 0.45$  throughout the paper. In the limit  $Y_e \rightarrow 0.5$  the SFP resonance moves significantly near the neutrinosphere and this can potentially change our conclusions regarding the detector response. The fluctuations are erased by the detector resolution because the relative phase acquired by the energy eigenstates from production to SFP resonance point is very large and therefore change rapidly with neutrino energy (see Eq. (40)). If SFP resonance comes closer to the neutrinosphere, it is possible that the relative phase becomes small and vary less with energy to create an observable effect. We believe that a systematic exploration of the dependence of SFP phase effect on the amount of overlap between SFP and MSW resonances is also important for the same reason. Another dimension that we did not explore is the effect of neutrino-neutrino interactions near the proto-neutron star. Neutrino-neutrino interaction potential creates additional resonances near the neutrinosphere which give rise to spectral splits [69, 70]. If these resonances are partially adiabatic [71], then they might have an effect on the energy dependence of the SFP phase as well. We leave these aspects of the problem to future publications.

### Acknowledgements

T. B. acknowledges the 2214A travel fellowship from the Scientific and Technological Research Council of Turkey (TÜBİTAK) and thanks the GSI Helmholtz Centre for Heavy Ion Research for their hospitality, where part of this work was carried out. Y.P. thanks to the organizers of the workshop on *Collective Neutrino Oscillations: From Quantum Information Science to Heavy Element Synthesis* at the Mainz Institute for Theoretical Physics, Johannes Gutenberg University, where she found an opportunity to discuss this work with many colleagues. Numerical calculations reported in this paper were partially performed at TÜBİTAK ULAKBİM High Performance and Grid Computing Center (TRUBA resources). This work was supported in part by a grant from Mimar Sinan Fine Arts University under project number 2018/48.

## References

- [1] W. Pauli, Relativistic Field Theories of Elementary Particles, *Rev.Mod.Phys.* 13 (1941) 203–232. doi:10.1103/RevModPhys.13.203.
- [2] B. W. Lee, R. E. Shrock, Natural Suppression of Symmetry Violation in Gauge Theories: Muon - Lepton and Electron Lepton Number Nonconservation, *Phys.Rev. D* 16 (1977) 1444. doi:10.1103/PhysRevD.16.1444.
- [3] R. E. Shrock, Electromagnetic properties and decays of dirac and majorana neutrinos in a general class of gauge theories, *Nuclear Physics B* 206 (3) (1982) 359–379. doi:https://doi.org/10.1016/0550-3213(82)90273-5. URL <https://www.sciencedirect.com/science/article/pii/0550321382902735>
- [4] K. Fujikawa, R. Shrock, The Magnetic Moment of a Massive Neutrino and Neutrino Spin Rotation, *Phys. Rev. Lett.* 45 (1980) 963. doi:10.1103/PhysRevLett.45.963.
- [5] A. B. Balantekin, N. Vassh, Magnetic moments of active and sterile neutrinos, *Phys. Rev. D* 89 (7) (2014) 073013. arXiv:1312.6858, doi:10.1103/PhysRevD.89.073013.
- [6] N. F. Bell, V. Cirigliano, M. J. Ramsey-Musolf, P. Vogel, M. B. Wise, How magnetic is the Dirac neutrino?, *Phys. Rev. Lett.* 95 (2005) 151802. arXiv:hep-ph/0504134, doi:10.1103/PhysRevLett.95.151802.
- [7] K. S. Babu, S. Jana, M. Lindner, Large neutrino magnetic moments in the light of recent experiments, *Journal of High Energy Physics* 2020 (10) (2020) 40. arXiv:2007.04291, doi:10.1007/JHEP10(2020)040.
- [8] P. Zyla, et al., Review of Particle Physics, *PTEP* 2020 (8) (2020) 083C01. doi:10.1093/ptep/ptaa104.
- [9] G. Raffelt, Limits on neutrino electromagnetic properties: An update, *Phys.Rept.* 320 (1999) 319–327. doi:10.1016/S0370-1573(99)00074-5.
- [10] C. Giunti, A. Studenikin, Neutrino electromagnetic interactions: a window to new physics, *Rev. Mod. Phys.* 87 (2015) 531. arXiv:1403.6344, doi:10.1103/RevModPhys.87.531.
- [11] M. B. Voloshin, M. I. Vysotsky, Neutrino Magnetic Moment and Time Variation of Solar Neutrino Flux, *Sov. J. Nucl. Phys.* 44 (1986) 544.
- [12] L. B. Okun, M. B. Voloshin, M. I. Vysotsky, Neutrino Electrodynamics and Possible Effects for Solar Neutrinos, *Sov. Phys. JETP* 64 (1986) 446–452.
- [13] C.-S. Lim, W. J. Marciano, Resonant Spin - Flavor Precession of Solar and Supernova Neutrinos, *Phys. Rev. D* 37 (1988) 1368–1373. doi:10.1103/PhysRevD.37.1368.
- [14] E. K. Akhmedov, Resonant Amplification of Neutrino Spin Rotation in Matter and the Solar Neutrino Problem, *Phys. Lett. B* 213 (1988) 64–68. doi:10.1016/0370-2693(88)91048-9.
- [15] L. Wolfenstein, Neutrino Oscillations in Matter, *Phys.Rev. D* 17 (1978) 2369–2374. doi:10.1103/PhysRevD.17.2369.
- [16] S. Mikheev, A. Y. Smirnov, Resonant amplification of neutrino oscillations in matter and solar neutrino spectroscopy, *Nuovo Cim. C9* (1986) 17–26. doi:10.1007/BF02508049.
- [17] S. J. Parke, Nonadiabatic level crossing in resonant neutrino oscillations, *PRL* 57 (10) (1986) 1275–1278. doi:10.1103/PhysRevLett.57.1275.
- [18] W. C. Haxton, Analytic Treatments of Matter Enhanced Solar Neutrino Oscillations, *Phys. Rev. D* 35 (1987) 2352. doi:10.1103/PhysRevD.35.2352.
- [19] S. P. Mikheev, A. Y. Smirnov, NEUTRINO OSCILLATIONS IN MATTER, in: *International Symposium on Weak and Electromagnetic Interactions in Nuclei*, 1987, pp. 405–415.
- [20] T.-K. Kuo, J. T. Pantaleone, Neutrino Oscillations in Matter, *Rev.Mod.Phys.* 61 (1989) 937. doi:10.1103/RevModPhys.61.937.
- [21] G. L. Fogli, E. Lisi, A. Mirizzi, D. Montanino, Analysis of energy and time dependence of supernova shock effects on neutrino crossing probabilities, *Phys. Rev. D* 68 (2003) 033005. arXiv:hep-ph/0304056, doi:10.1103/PhysRevD.68.033005.
- [22] J. P. Kneller, G. C. McLaughlin, Monte Carlo neutrino oscillations, *Phys. Rev. D* 73 (2006) 056003. arXiv:hep-ph/0509356, doi:10.1103/PhysRevD.73.056003.
- [23] J. P. Kneller, G. C. McLaughlin, J. Brockman, Oscillation Effects and Time Variation of the Supernova Neutrino Signal, *Phys. Rev. D* 77 (2008) 045023. arXiv:0705.3835, doi:10.1103/PhysRevD.77.045023.
- [24] S. Galais, J. Kneller, C. Volpe, J. Gava, Shockwaves in Supernovae: New Implications on the Diffuse Supernova Neutrino Background, *Phys. Rev. D* 81 (2010) 053002. arXiv:0906.5294, doi:10.1103/PhysRevD.81.053002.
- [25] J. P. Kneller, C. Volpe, Turbulence effects on supernova neutrinos, *Phys. Rev. D* 82 (2010) 123004. arXiv:1006.0913, doi:10.1103/PhysRevD.82.123004.
- [26] S. Horiuchi, J. P. Kneller, What can be learned from a future supernova neutrino detection?, *J. Phys. G* 45 (4) (2018) 043002. arXiv:1709.01515, doi:10.1088/1361-6471/aaa90a.
- [27] B. Dasgupta, A. Dighe, Phase effects in neutrino conversions during a supernova shock wave, *Phys. Rev. D* 75 (2007) 093002. arXiv:hep-ph/0510219, doi:10.1103/PhysRevD.75.093002.
- [28] L. D. Landau, To the theory of energy transmission in collisions. II, *Phys. Zs. Sowjet* 2 (1932) 46.
- [29] C. Zener, Non-Adiabatic Crossing of Energy Levels, *Proceedings of the Royal Society of London Series A* 137 (833) (1932) 696–702. doi:10.1098/rspa.1932.0165.
- [30] J. R. Rubbmark, M. M. Kash, M. G. Littman, D. Kleppner, Dynamical effects at avoided level crossings: A study of the Landau-Zener effect using Rydberg atoms, *Physical Review A* 23 (6) (1981) 3107–3117. doi:10.1103/physreva.23.3107. URL <https://ui.adsabs.harvard.edu/abs/1981PhRvA...23.3107R>
- [31] A. Y. Smirnov, The MSW effect and matter effects in neutrino oscillations, *Phys. Scripta T* 121 (2005) 57–64. arXiv:hep-ph/0412391, doi:10.1088/0031-8949/2005/T121/008.
- [32] Y. Kayanuma, Role of phase coherence in the transition dynamics of a periodically driven two-level system, *Phys. Rev. A* 50 (1994) 843–845. doi:10.1103/PhysRevA.50.843. URL <https://link.aps.org/doi/10.1103/PhysRevA.50.843>
- [33] Y. Kayanuma, Stokes phase and geometrical phase in a driven two-level system, *Phys. Rev. A* 55 (1997) R2495–R2498. doi:10.1103/PhysRevA.55.R2495. URL <https://link.aps.org/doi/10.1103/PhysRevA.55.R2495>
- [34] S. E. Woosley, A. Heger, T. A. Weaver, The evolution and explosion of massive stars, *Reviews of Modern Physics* 74 (2002) 1015–1071. doi:10.1103/RevModPhys.74.1015.
- [35] K. Kotake, K. Sato, K. Takahashi, Explosion mechanism, neutrino burst, and gravitational wave in core-collapse supernovae, *Rept.Prog.Phys.* 69 (2006) 971–1144. arXiv:astro-ph/0509456, doi:10.1088/0034-4885/69/4/R03.
- [36] H.-T. Janka, K. Langanke, A. Marek, G. Martinez-Pinedo, B. Mueller, Theory of Core-Collapse Supernovae, *Phys.Rept.* 442 (2007) 38–74. arXiv:astro-ph/0612072, doi:10.1016/j.physrep.2007.02.002.
- [37] K. Nomoto, T. Shigeeyama, M.-A. Hashimoto, Hydrodynamical models of supernova 1987A in the Large Magellanic Cloud, in: I. J. Danziger (Ed.), *European Southern Observatory Conference and Workshop Proceedings*, Vol. 26 of *European Southern Observatory Conference and Workshop Proceedings*, 1987, pp. 325–346.
- [38] A. Ahrliche, J. Mimouni, Supernova neutrino spectrum with matter and spin flavor precession effects, *JCAP* 11 (2003) 004. arXiv:astro-ph/0306433, doi:10.1088/1475-7516/2003/11/004.
- [39] Y. Pehlivan, A. B. Balantekin, T. Kajino, Neutrino Magnetic Moment, CP Violation and Flavor Oscillations in Matter, *Phys.Rev. D* 90 (6) (2014) 065011. arXiv:1406.5489, doi:10.1103/PhysRevD.90.065011.
- [40] A. de Gouvêa, S. Shalgar, Effect of transition magnetic moments on collective supernova neutrino oscillations, *JCAP* 2012 (10) (2012) 027. arXiv:1207.0516, doi:10.1088/1475-7516/2012/10/027.
- [41] A. de Gouvêa, S. Shalgar, Transition magnetic moments and collective neutrino oscillations: three-flavor effects and detectability, *JCAP* 2013 (4) (2013) 018. arXiv:1301.5637, doi:10.1088/1475-7516/2013/04/018.
- [42] O. G. Kharlanov, P. I. Shustov, Effects of nonstandard neutrino self-interactions and magnetic moment on collective Majorana neutrino oscillations, *Phys. Rev. D* 103 (9) (2021) 095004. arXiv:2010.05329, doi:10.1103/PhysRevD.103.095004.
- [43] H. Sasaki, T. Takiwaki, Neutrino-antineutrino oscillations induced by strong magnetic fields in dense matter, *Phys. Rev. D* 104 (2) (2021) 023018. arXiv:2106.02181, doi:10.1103/PhysRevD.104.023018.

- [44] H. Sawai, K. Kotake, S. Yamada, The Core-collapse supernova with non-uniform magnetic fields, *Astrophys. J.* 631 (2005) 446–455. [arXiv:astro-ph/0505611](#), doi:10.1086/432529.
- [45] E. G. Flowers, P. G. Sutherland, Neutrino Neutrino Scattering and Supernovae, *Astrophys. J. Lett.* 208 (1976) L19–L21. doi:10.1086/182223.
- [46] G. M. Fuller, R. W. Mayle, J. R. Wilson, D. N. Schramm, Resonant neutrino oscillations and stellar collapse, *APJ* 322 (1987) 795–803. doi:10.1086/165772.
- [47] J. T. Pantaleone, Neutrino oscillations at high densities, *Phys.Lett.* B287 (1992) 128–132. doi:10.1016/0370-2693(92)91887-F.
- [48] J. T. Pantaleone, Dirac neutrinos in dense matter, *Phys.Rev.* D46 (1992) 510–523. doi:10.1103/PhysRevD.46.510.
- [49] H. Duan, G. M. Fuller, Y.-Z. Qian, Collective Neutrino Oscillations, *Ann.Rev.Nucl.Part.Sci.* 60 (2010) 569–594. [arXiv:1001.2799](#), doi:10.1146/annurev.nucl.012809.104524.
- [50] S. Chakraborty, R. Hansen, I. Izaguirre, G. Raffelt, Collective neutrino flavor conversion: Recent developments, *Nucl. Phys.* B908 (2016) 366–381. [arXiv:1602.02766](#), doi:10.1016/j.nuclphysb.2016.02.012.
- [51] M. C. Volpe, Neutrinos from dense: flavor mechanisms, theoretical approaches, observations, new directions (1 2023). [arXiv:2301.11814](#).
- [52] H. Duan, G. M. Fuller, J. Carlson, Y.-Z. Qian, Simulation of Coherent Non-Linear Neutrino Flavor Transformation in the Supernova Environment. I. Correlated Neutrino Trajectories, *Phys.Rev.* D74 (2006) 105014. [arXiv:astro-ph/0606616](#), doi:10.1103/PhysRevD.74.105014.
- [53] A. Friedland, Do solar neutrinos constrain the electromagnetic properties of the neutrino?, [arXiv e-prints](#) (May 2005). [arXiv:hep-ph/0505165](#).
- [54] A. Y. Smirnov, The MSW effect and solar neutrinos, in: 10th International Workshop on Neutrino Telescopes, 2003, pp. 23–43. [arXiv:hep-ph/0305106](#).
- [55] C. Giunti, C. Kim, U. Lee, Coherence of neutrino oscillations in vacuum and matter in the wave packet treatment, *Physics Letters B* 274 (1) (1992) 87 – 94. doi:[https://doi.org/10.1016/0370-2693\(92\)90308-q](https://doi.org/10.1016/0370-2693(92)90308-q). URL <http://www.sciencedirect.com/science/article/pii/037026939290308q>
- [56] R. Sloth Lundkvist Hansen, A. Y. Smirnov, The Liouville equation for flavour evolution of neutrinos and neutrino wave packets, *JCAP* 2016 (12) (2016) 019. [arXiv:1610.00910](#), doi:10.1088/1475-7516/2016/12/019.
- [57] C. Giunti, *Fundamentals of Neutrino Physics and Astrophysics*, Oxford University Press, 2007.
- [58] S. Nussinov, Solar Neutrinos and Neutrino Mixing, *Phys. Lett. B* 63 (1976) 201–203. doi:10.1016/0370-2693(76)90648-1.
- [59] J. Pulido, The solar neutrino problem and the neutrino magnetic moment, *Physics Reports* 211 (4) (1992) 167–199. doi:10.1016/0370-1573(92)90071-7.
- [60] H. Nunokawa, Y. Z. Qian, G. M. Fuller, Resonant neutrino spin flavor precession and supernova nucleosynthesis and dynamics, *Phys. Rev. D* 55 (1997) 3265–3275. [arXiv:astro-ph/9610209](#), doi:10.1103/PhysRevD.55.3265.
- [61] A. Dar, Neutrino Magnetic Moment May Solve the Supernovae Problem (2 1987).
- [62] A. V. Kuznetsov, N. V. Mikheev, A. A. Okrugin, Dirac-Neutrino Magnetic Moment and the Dynamics of a Supernova Explosion, *JETP Lett.* 89 (2009) 97–101. [arXiv:0903.2321](#), doi:10.1134/S0021364009030011.
- [63] A. K. Alok, N. R. Singh Chundawat, A. Mandal, T. Sarkar, Can neutron star discriminate between Dirac and Majorana neutrinos? (8 2022). [arXiv:2208.02239](#).
- [64] B. Abi, et al., Supernova neutrino burst detection with the Deep Underground Neutrino Experiment, *Eur. Phys. J. C* 81 (5) (2021) 423. [arXiv:2008.06647](#), doi:10.1140/epjc/s10052-021-09166-w.
- [65] P. Huber, M. Lindner, W. Winter, Simulation of long-baseline neutrino oscillation experiments with GLoBES (General Long Baseline Experiment Simulator), *Comput. Phys. Commun.* 167 (2005) 195. [arXiv:hep-ph/0407333](#), doi:10.1016/j.cpc.2005.01.003.
- [66] P. Huber, J. Kopp, M. Lindner, M. Rolinec, W. Winter, New features in the simulation of neutrino oscillation experiments with GLoBES 3.0: General Long Baseline Experiment Simulator, *Comput. Phys. Commun.* 177 (2007) 432–438. [arXiv:hep-ph/0701187](#), doi:10.1016/j.cpc.2007.05.004.
- [67] H. Snowglobes code: Supernova observatories with globes, <https://github.com/snowglobes/snowglobes> (2023). URL <https://github.com/SNOwGLoBES/snowGlobes>
- [68] S. Amoroso, et al., Measurement of the mu decay spectrum with the ICARUS liquid argon TPC, *Eur. Phys. J. C* 33 (2004) 233–241. [arXiv:hep-ex/0311040](#), doi:10.1140/epjc/s2004-01597-7.
- [69] G. G. Raffelt, A. Y. Smirnov, Self-induced spectral splits in supernova neutrino fluxes, *Phys. Rev. D* 76 (2007) 081301, [Erratum: *Phys.Rev.D* 77, 029903 (2008)]. [arXiv:0705.1830](#), doi:10.1103/PhysRevD.76.081301.
- [70] G. G. Raffelt, A. Y. Smirnov, Adiabaticity and spectral splits in collective neutrino transformations, *Phys. Rev. D* 76 (2007) 125008. [arXiv:0709.4641](#), doi:10.1103/PhysRevD.76.125008.
- [71] B. Ekinci, Y. Pehlivan, A. V. Patwardhan, Time dependent signatures of core-collapse supernova neutrinos at HALO, *Phys. Rev. D* 103 (4) (2021) 043016. [arXiv:2101.01797](#), doi:10.1103/PhysRevD.103.043016.